

Ice fabrics in natural two-dimensional flows: beyond pure and simple shear

Daniel H. M. Richards¹, Samuel S. Pegler², and Sandra Piazzolo³

¹Fluid Dynamics CDT, University of Leeds, United Kingdom

²School of Mathematics, University of Leeds, United Kingdom

³School of Earth and Environment, University of Leeds, United Kingdom

Correspondence: Daniel H. M. Richards (scdhmr@leeds.ac.uk)

Abstract. Ice fabrics are key for understanding and predicting ice flow dynamics. Despite its importance, the characteristics and evolution of ice fabrics beyond pure and simple shear flow has largely been neglected. However, 80% of the flow of ice in Antarctica is Within an ice sheet, a significant part of the deformation can be outside the regimes of pure and simple shear. We use a new validated recently developed numerical model (SpecCAF), which has been shown to accurately reproduce experimentally observed fabrics in both compression and simple shear, to explore classify the fabrics produced between under general two-dimensional deformation regimes. Our analysis develops the first predictions for fabric patterns arising over a continuous spectrum of incompressible two-dimensional deformation regimes and temperatures, encompassing those intermediate to pure and simple shear, as well as those that are highly rotational. We present a definitive classification of all fabric patterns. We more rotational than simple shear. We find that intermediate deformations deformation regimes between pure and simple shear result in a smooth transition between a fabric characterised by a cone-shape and a secondary cluster pattern. Highly-rotational fabrics are found deformation regimes are revealed to produce a weak girdle fabric. In addition we obtain complete, we obtain predictions for the strain required for any fabric under a 2D deformation to reach steady state strain-scales over which fabric evolution takes place at any given temperature. Use of our data in current The use of our model in large-scale ice flow models as well as for ice core fabric interpreting fabrics observed in ice cores and seismic anisotropy interpretation will enhance the communities' ability to predict future, will provide new tools supporting the community in predicting ice flow in a changing climate.

1 Introduction

Mass loss from ice sheets is set to be the main contributor to sea-level rise this century (e.g. Shepherd et al., 2018). Reliably predicting sea-level rise depends on accurately modelling ice flow. One of the most important controls on ice flow dynamics is the ice fabric, i.e. the arrangement of ice grains in terms of their crystallographic axes. Strong alignment of the crystal lattices may cause the strain-rate response to an applied stress to vary by a factor of 9 in different directions (e.g. Pimienta and Duval, 1987). Hence, understanding the fabrics present in any flowing ice sheet, i.e. Antarctica or Greenland, is important for predicting ice-sheet flow and, in turn, the loss of ice over time.

There are a number of issues that need to be resolved before it is possible to fully interpret ice fabrics To date, the analysis and discussion of ice fabrics has focused primarily on those formed under the specific deformation regimes of pure and simple shear. The primary

25 motivation of the present paper is to use the validated fabric model SpecCAF (Richards et al., 2021) to take a step away
from the isolated conditions of pure and simple shear and explore the continuous space of deformation regimes lying
intermediate to these endmember cases, and also those that are more rotational than simple shear, across a unified
spectrum. Ice flow is commonly modelled in the two-dimensional x - z plane (e.g Martín et al., 2009), and analysis of this
30 in section 2.2.1 below). Therefore, an exploration of the fabric patterns arising in this generalised situation is necessary
as a step towards improving our ability to interpret fabrics derived from ice cores and to be able to predict future ice flow taking
ice fabric effects into account. Firstly, it is unknown what deformations are important in the natural world, for example the Antarctic ice-sheet. Secondly, if deformation
regimes that have not been studied in experiments are common in the natural world, As a first step towards this, we seek here to address a number of
open questions. First, what fabrics are produced from these deformations? It is also unknown how under any given (incompressible) two-
35 dimensional deformation regime? Second, how do fabrics evolve at the very high strains which cannot be explored in experiments.
Furthermore, have remained inaccessible to laboratory experiments? Third, what strains are necessary to reach steady state
in the different deformation regimes? Finally, at these high strains, how is the final steady-state are the final steady states dependent
on parameters such as temperature and type of deformation , and can it be reached in the natural world? By exploring the predictions of a recently developed
experimentally constrained continuum model for ice fabrics (Richards et al., 2021), we will address each of these questions. regime?

40 2 Background

2.1 Fabric Development

2.1.1 Processes governing fabric development

The distribution of crystallographic orientations within a polycrystal is called the fabric or crystallographic preferred orientation
(CPO). Due to the dominance of basal slip Basal-slip is generally dominant in ice (Duval et al., 1983), it is sufficient to consider the orientation changes
45 through time of the normal to the basal plane, referred to as the although non-basal slip systems are active, especially at high temperatures
(Chauve et al., 2017). To leading order the distribution of the c -axis, alone, -axes is the key control for the mechanical properties
(e.g. viscous anisotropy) of ice (Duval, 1981). As ice flows, the under deformation by crystal plasticity, the distribution of
 c -axes align evolves to produce a fabric from the combination of deformation and recrystallization. There are four main processes which affect the fabric: basal-
slip deformation , migration . The intensity of the fabric, and the pattern seen, is dependent on the conditions of deformation
50 which will influence the relative activity of different deformation mechanisms. During crystal plasticity several deformation
mechanisms may be active. These include crystal slip, grain boundary migration (also termed migration recrystallization),
rotational recrystallization , and rigid-body rotation and rotational recrystallization . Basal-slip deformation can be understood through the analogy of a deck
of cards sliding over one another causing rotation. Crystal slip occurs predominantly by slip along the basal plane, which results in
a systematic change in orientation of the c -axes to rotate towards the axis of compression (Azuma and Higashi, 1984; van der Veen and Whillans, 1994).
55 Migration recrystallization is the process whereby grains with a lower dislocation density grow into neighbouring grains with higher dislocation density. The dislocation density
at a specific grain is primarily caused by the stress imposed on the -axis (Steinemann, 1958; Hondoh, Takeo, 2000), even though other slip

systems are activated to a minor degree if deformed at high temperatures (Chauve et al., 2017) and in areas of local stress heterogeneities (Piazolo et al., 2015).

60 Migration recrystallization in a deforming crystalline material that deforms by crystal plasticity is mainly driven by difference in strain energy i.e. energy related to unbound dislocation density either side of a grain, which is dependent on the orientation of that grain relative to the deformation. As a consequence of the stress on the grain, dislocations appear and grow. Depending boundary (e.g. Humphreys and Hatherly, 2004). Hence, in the case of such strain induced migration recrystallization (Drury et al., 1985; Drury and Urai, 1990) the less strained grain grows at the expense of the more strained grain resulting in an overall decrease in the strain energy of the system. As the strain energy stored in a grain (i.e. dislocation density) is directly related to the imposed stress (Gottstein and Shvindlerman, 1999) migration recrystallization is inherently related to stress as well. The
65 dislocation density accumulated within a certain grain is primarily a response to its orientation relative to the main deviatoric stress axes. For example, a grain favourably oriented for basal slip will accumulate less dislocations than a grain that is oriented unfavourably. Consequently, depending on the deformation, grains at certain orientations regime, grains of certain orientation will grow at the expense of others. Therefore grains of another unfavourable orientation. As a result, the effect of migration recrystallization is to produce c-axes c-axes clustered towards certain orientations in the polycrystal. a polycrystal. Even
70 though some studies suggest that fabric is stress-dependent (Harte et al., 2020; Hudleston, 2015), the effect of migration recrystallization will be the same on the resulting fabric.

Rotational recrystallization occurs where sub-grains form close to the when dislocations recover into subgrain boundaries which, with increasing strain, will develop into grains (Drury et al., 1985). As dislocations are concentrated close to grain bound-
75 aries due to localised stress concentrations (Drury and Urai, 1990). stress heterogeneities (Piazolo et al., 2015), subgrains, and therefore new grains developing from subgrains, dominantly occur near grain boundaries. The orientation of these new grains is random to leading order. This acts to diffuse any concentrations of the c-axis towards a particular orientation -axes of the original grain (Gödert, 2003). Rigid-body rotation acts to rotate any grain and therefore its c-axes according to -axis in accordance with the rotational characteristics of the deformation regime that the ice grains are subjected to.

80 2.1.2 Observed fabrics

Ice fabrics can be observed through laboratory experiments, the taking of through ice cores from real-world locations, and more recently, more recently, inferred through seismic measurements.

In the laboratory, the majority of experiments are performed in compression, either in pure shear (2D) or unconfined (uniaxial) compression (3D), without any rotational component (Jacka and Maccagnan, 1984; Jacka, 2000; Craw et al., 2018; Fan et al., 2020; Piazolo et al.,
85 2013) and others (e.g. Jacka and Maccagnan, 1984; Jacka, 2000; Craw et al., 2018; Fan et al., 2020; Piazolo et al., 2013). The other end-member endmember considered is simple-shear (Journaux et al., 2019; Qi et al., 2019). Wilson and Peterzell (2012) is the only work exploring intermediate deformations, focusing mainly on the strain-rate response. Laboratory experiments provide detailed fabric measurements in known conditions. However experiments are limited to mostly limited to endmember deformation regimes, as well as to strains of around 0.4 for compression (Fan et al., 2020) and 2 for direct simple shear (Qi et al., 2019).

90 **Analysis of fabrics** Experiments have been performed using combined compression and shear, at close to the melting point of ice (Duval, 1981; Jun et al., 1996; Budd et al., 2013). Fabrics from Duval (1981) combining unconfined compression and simple shear show a broad cluster with 3 or 4 maxima inside it. Budd et al. (2013) shows, for an experiment with mostly simple shear combined with some confined compression and at an equivalent strain to that used later in this paper of 0.75, a fabric which shows the merging of a double cluster (from pure shear) and a single-maxima (from simple shear). Experiments have also been performed with layered samples of ice (Wilson, 2000; Wilson and Peterzell, 2012). In addition to the relatively few experiments that have been conducted under a combination of simple and pure shear, no analysis has been conducted of situations where fabrics are produced in deformation regimes more rotational than simple shear. We show in section 2.2.2 that deformation regimes inbetween pure and simple shear, and those more rotational than simple shear, occur widely in natural ice-sheet flows.

100 Fabrics can also be **done analysed** by taking ice cores in **real world locations**. **ice sheets**. An understanding of the fabrics enables us to interpret the deformation regime and temperature history of ice cores. Initial studies of ice cores have concentrated on ice domes or divides (Gow, 1961; Holtzschcher et al., 1954; Johnsen et al., 1995). These locations are deliberately chosen because they have minimal deformation, to act as a good proxy for past climate data. At domes, the ice will be deformed vertically in unconfined compression, producing either a single-maximum or a girdle shape fabric , as shown in (Fig. 1). Recently, ice cores have become available in locations with more complex deformation **histories** (?Treverrow et al., 2010). ? **regime histories** (Stoll et al., 2018; Treverrow et al., 2010). Stoll et al. (2018) show examples of a variety of fabric shapes such as girdles and single-maximum fabrics orientated in different directions as well as relatively faster fabric development with depth compared to ice cores at domes. An understanding of the fabrics produced in different conditions could enable us to better understand the deformation and temperature history of ice cores. Fabrics can also be measured from boreholes using **more recent** sonic and optical **measurements** (Klusiewicz et al., 2017; Rongen et al., 2020) **techniques** (Gusmeroli et al., 2012; Klusiewicz et al., 2017).

110 Recently, data from radar and seismics has also been used to infer fabric properties (Matsuoka et al., 2003; Fujita et al., 2006; Booth et al., 2020). These methods can capture natural ice fabrics without expensive drilling, allowing data to be collected at more active locations such as ice streams (Jordan et al., 2020).

2.1.3 Fabric **patterns**development

115 Figure 1 **shows** **illustrates schematically** some commonly observed CPO patterns seen in **laboratory** experiments and from ice cores. These are illustrated by pole figures which show half of the of c -axis orientations (which cover the space of a unit sphere) projected onto a plane . As (since the c -axes are antipodally symmetric, this is sufficient to show all the information). Laboratory experiments studying CPO evolution have been performed mostly in uniaxial compression and this produces either a single maximum at low temperatures (Fig. 1a) or a cone-shape fabric at high temperatures (Fig. 1b). At low **temperature** **temperatures** ($T \approx -30^\circ \text{C}$) basal-slip deformation **regime** dominates and this causes c -axes to rotate towards the axis of compression, producing the single-maximum **shown** in Fig. 1a. The cone-shape fabric **shown** in Fig. 1b, **seen in experiments such as** Kamb (1972). is produced by the balance of basal-slip deformation **regime** and migration recrystallization. The process of migration recrystallization acts to consume grains orientated towards the compression axis, and grow grains orientated in a ring

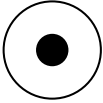



Fabric name	(a) Single-maximum	(b) Cone-shape	(c) Double-maximum	(d) Secondary cluster
Pole figure				
Deformation	Compression, Simple shear	Unconfined compression	Confined compression	Simple shear
Temperature	Low (~ -30°C)	High (~ -10°C)	High (~ -10°C)	High (~ -10°C)

Figure 1. Illustration showing common fabrics or CPOs which develop in ice, illustrated by their pole figures, as well as the deformation regime and temperature they typically occur at. The pole figures show the distribution of c -axis orientations, with the compression axis at the centre. (a) shows a single-maximum fabric, produced in unconfined compression or simple shear at low temperatures (Qi et al., 2019). (b) shows a cone-shape fabric, produced in unconfined compression at higher temperatures, when grain-boundary migration is active (Paterson, 1999). This can also be considered a girdle fabric when the cone-angle approaches 90° . (c) shows a double maxima fabric produced in confined compression (pure shear) (Budd et al., 2013). (d) shows a single-maximum with a secondary cluster, produced in simple shear at higher temperatures (Qi et al., 2019)(Kamb, 1972; Qi et al., 2019).

125 45° away from the compression axis. Therefore, the balance of basal-slip deformation regime and migration recrystallization produces a ring or cone-shape pattern in the pole figure. In pure shear, which is a 2D compression, the grains produced by migration recrystallization do not form a ring but rather instead form two clusters at 45° , hence the double-maxima fabric as shown in Fig. 1c is produced rather than a cone-shape fabric. This has been seen in experiments such as Budd et al. (2013).

130 Recent simple shear experiments produce either a single-maximum at low temperatures, or a single-maximum with an offset secondary cluster (Fig. 1d) at intermediate strains and high temperatures (Qi et al., 2019; Journaux et al., 2019). This pattern is similar to a double-maxima but the presence of vorticity in simple shear deformations causes the cluster that is not aligned with the shear plane normal to be advected towards the primary cluster. As the secondary cluster's orientation changes, grains of that orientation accumulate more dislocations so start to be consumed by migration recrystallization. This results in the imbalance in cluster strengths seen in Fig. 1d.

2.2 Flow Classifying flow regimes

135 2.2.1 General deformations There exist deformation regimes

There exists a significant variety of deformations deformation regimes in the natural world. One way to classify a deformation regime is by the vorticity number (Passchier, 1991), which measures the ratio of vorticity magnitude to shearing strain-rate magnitude:

$$\mathcal{W} = \sqrt{\frac{W_{ij}W_{ij}}{D_{ij}D_{ij}}}, \quad (1)$$

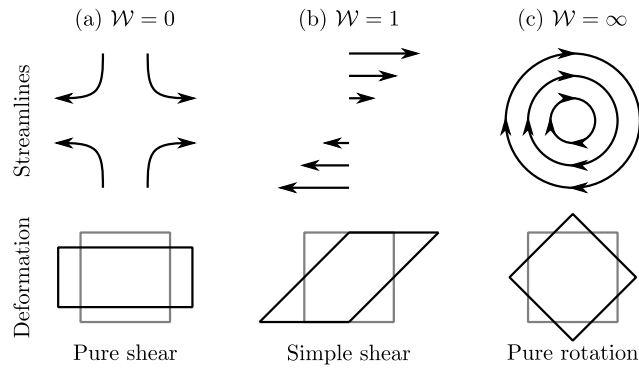


Figure 2. Schematics illustrating two-dimensional flow regimes at different vorticity numbers \mathcal{W} (Eq. (1)): (a) Pure shear ($\mathcal{W} = 0$), (b) Simple shear ($\mathcal{W} = 1$), (c) Pure rotation ($\mathcal{W} = \infty$). For each flow the streamlines and deformation regime produced are shown.

140 where $\mathbf{W} = \frac{1}{2}(\nabla\mathbf{u} - \nabla\mathbf{u}^T)$ is the anti-symmetric part of the velocity gradient (the spin-rate tensor) and $\mathbf{D} = \frac{1}{2}(\nabla\mathbf{u} + \nabla\mathbf{u}^T)$ is the symmetric part of the velocity gradient (the strain-rate tensor). Figure 2 illustrates different flow regimes and the corresponding vorticity number \mathcal{W} for each. The vorticity number is 0 for pure shear or uniaxial compression, 1 for simple shear and ∞ for rigid-body rotation. Ice in the natural world will experience **deformations** **deformation regimes** with vorticity numbers from 0 to ∞ , however to date fabrics produced for $\mathcal{W} = 0$ and $\mathcal{W} = 1$ are the only areas which have been extensively explored
 145 due to the limitations of possible **deformations** **deformation regimes** in experiments.

In geology, numerous studies have shown that in the natural world the full range of different deformation regimes occur (Jiang, 1994; Bailey and Eyster, 2003). Such studies have been supported by theoretical (Fossen and Tikoff, 1993; Tikoff and Fossen, 1995) and analogue modelling (Piazolo et al., 2002, 2004), (ten Grotenhuis et al., 2002). **the** late 1990s and early 2000s it was recognised in the geological community that flow in rocks cannot be approximated by endmember plane strain flow models alone (Jiang, 1994; Bailey and Eyster, 2003). There is now an extensive literature
 150 within structural geology which developed conceptual models and analytical techniques to predict and recognise natural geological flows with vorticity numbers between 0 and 1 (Fossen and Tikoff, 1993; Tikoff and Fossen, 1995; Piazolo et al., 2002, 2004; ten Grotenhuis et al., 2002) In contrast, such analysis is less common in discussions surrounding ice core interpretation; pure shear and simple shear tend to dominate discussions regarding both the interpretation of ice-sheet flow and experimental analysis. This may be mainly due to the fact that such endmember scenarios are a) experimentally
 155 straightforward to achieve, b) the two endmembers can – as a first approximation - be associated with different ice flow scenarios of an ice divide and the shallow ice approximation (although the shallow ice approximation is only in simple shear towards the base).

2.2.2 Two-dimensional deformation regimes in natural ice flow

As a first step towards exploring the fabrics produced by all possible deformation regimes, we will focus here on general in-
 160 compressible two-dimensional deformations. Although deformation regimes in the natural world will be three-dimensional, exploring fabrics produced by two-dimensional deformation regimes is a natural first step away from the canonical regimes

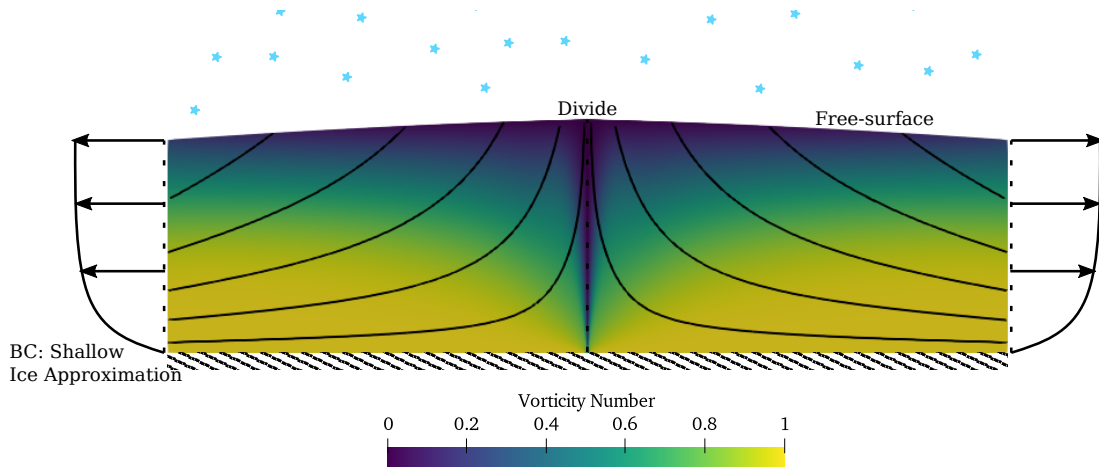


Figure 3. Schematic illustrating flow regimes at different vorticity numbers \mathcal{W} (Eq. 1): (a) Pure shear ($\mathcal{W} = 0$) divide, (b) Simple shear ($\mathcal{W} = 1$) showing a range from 0 to 1. The problem setup is from Martín et al. (2009) with isotropic ice. The simulation has an aspect ratio of 20, (c) Pure rotation ($\mathcal{W} = \infty$) but only the region from $x = 0$ to $x = 10H$, where H is the height of model domain, is shown. For each flow regime the domain has the streamlines velocity from the shallow-ice-approximation imposed at the left and right boundaries, and the surface accumulation is set to match the outflow, corresponding to a steady state. No-slip is imposed at the base and a free surface is assumed at the top. The vorticity number is shown, alongside streamlines. In experiments only pure shear have been considered extensively solved using Taylor-Hood elements.

of pure and simple shear. It is also common to limit the modelling of ice-sheet to two dimensions, in the vertical cross-section (Pattyn et al., 2008; Martín et al., 2009). In Fig. 3, we show the vorticity number from a 2D simulation of flow at an ice divide and its horizontal transition towards a flow dominated by vertical shear stresses (the shallow ice approximation). Due to the vanishing of horizontal velocity at the divide, the vorticity number is 0 there, corresponding to the regime of pure shear along $x = 0$. Away from the divide, the flow dominated by vertical shear stresses exhibits a transition in the vorticity number from 1 at the base, corresponding to simple shear, towards close to 0 at the surface. In summary, the figure shows vorticity numbers between 0 and 1 are the norm.

2.2.3 Deformations in the natural world

170 By an analogy to geology (Beam and Fisher, 1999; Xypolias, 2010) we expect a variety of deformations are likely

It is not only vorticity numbers between 0 and 1 which can occur. Vorticity numbers greater than 1, corresponding to deformation regimes more rotational than simple shear, are predicted to occur in natural ice flow. To test this hypothesis, ice sheets. As an example consider the flow of ice over a Gaussian bump at the base shown in Fig. 4. This is modification of the ISMIP-HOM experiment F benchmark (Pattyn et al., 2008), representing ice flowing downhill over a Gaussian bump. Compared to Pattyn et al. (2008), the bump is 4 times higher and 31.6 times sharper. This shows even in a simple configuration,

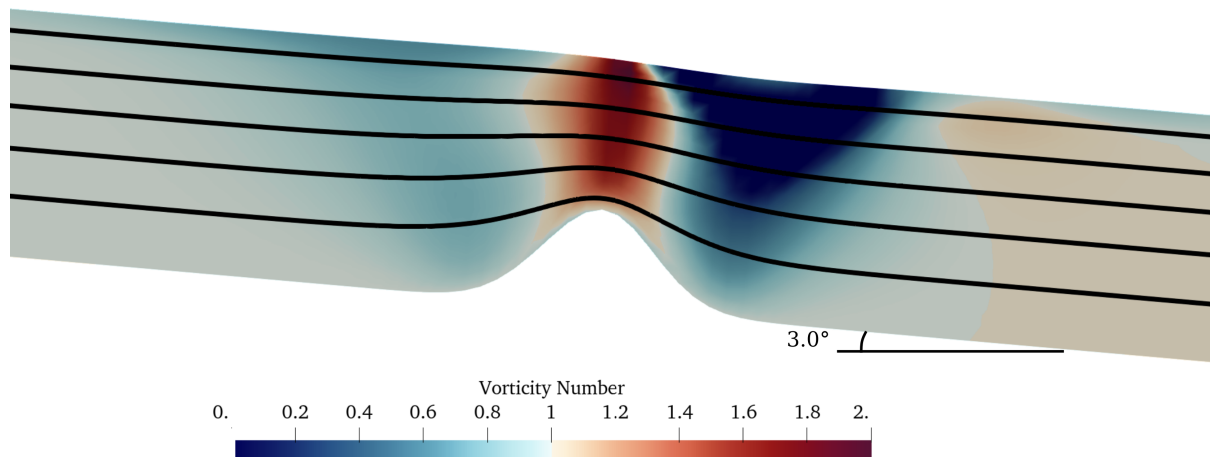


Figure 4. The vorticity number for a 2D slice from a modified version of the ISMIP-HOM Experiment F benchmark (Pattyn et al., 2008). The ice is flowing from left to right, down a hill with angle 3.0° , and encounters a Gaussian bump at the base. Compared to Pattyn et al. (2008), the Gaussian bump is 4 times higher and 31.6 times sharper. Over the bump the flow accelerates leading to vorticity numbers greater than 1. This simulation was performed using Elmer/ICE (Gagliardini et al., 2013) with $n = 1$.

vorticity numbers greater than 1 can potentially occur in the vertical velocity profile. Fig. 4 shows vorticity numbers up to 2. To-date, the fabrics produced for vorticity numbers above 1 have not been analysed.

Further, we have calculated an estimate of the vorticity number near the surface of Antarctica, in order to illustrate the natural deviation from endmember regimes. To do this we have used surface velocity data from Antarctica (Mouginot et al., 2019) to calculate the surface vorticity number, shown in Fig. 5. We have calculated the surface velocity gradients $\partial u/\partial x, \partial u/\partial y, \partial v/\partial x, \partial v/\partial y$ using central differencing. To evaluate the vorticity number, we use these estimates of horizontal velocity gradients combined with an estimate of the maximum vertical shear ($\partial u/\partial z, \partial v/\partial z$) in the top 25% of the depth of the ice-sheet determined using the shallow-ice approximation assuming no basal-slip. The derivative $\partial w/\partial z$ is calculated using mass continuity and we have neglected the higher order contributions $\partial w/\partial x$ and $\partial w/\partial y$.

To reduce the errors in the data for Fig. 5 we have taken the mean value from a 10×10 block (covering a 4.5 km square). We have defined the standard deviation of any variables, such as velocity components, as the variance from the mean of the 100 samples in each 10×10 block. The relative standard deviation controls the transparency: if this is $> 100\%$ this location is plotted as white, and a relative standard deviation of 0% is plotted as the full colour. From this figure we can see that there are many regions of Antarctica where the surface vorticity number vorticity number near the surface is both at intermediate values between 0 and 1, and many areas where $\mathcal{W} > 1$ greater than 1. The regions characterised by high vorticity numbers ($\mathcal{W} > 1$) typically shown to occur in the regions of ice streamswith curved streamlines.

Figure ??a shows a cumulative distribution plot of the surface vorticity numbers present in Fig. 5 and Fig. ??b shows the corresponding distribution plot (the derivative of ??a). Both plots highlight the difference in the distribution between all velocity magnitudes, and the fastest and slowest 5%. From this we can see that intermediate deformations ($0.1 < \mathcal{W} < 0.9$) are very common, accounting for around 70% of the deformations. Figure ??b shows that slow speeds are dominated by vorticity numbers close to 0.4, i.e. with

195 a significant pure shear component. This is contrasted by the fastest 5% which are dominated by simple shear ($\mathcal{W} = 1$). Highly rotational regions ($\mathcal{W} > \infty$) are also important, as they are common in the fastest regions : 40% of the deformations with occur typically in highly dynamic regions such as ice streams. Closer to the base of an ice-sheet, the fastest 5% of speeds have $\mathcal{W} > 1$ vorticity number tends to 1 as the vertical gradients dominate. In regions with no basal slip, these vorticity numbers are potentially valid to approximately 25% into the ice-sheet. In regions with basal slip, the vorticity number will be valid deeper into the ice-sheet.

200 Distribution of surface vorticity numbers of Antarctica, shown in Fig. 5. (a) shows the cumulative distribution and (b) shows the derivative of this, the distribution plot. For both, the distribution is shown for all speeds, the fastest 5% ($|\mathbf{u}| > 404 \text{ ma}^{-1}$) and the slowest 5% ($|\mathbf{u}| < 0.83 \text{ ma}^{-1}$).

2.3 Modelling Hierarchy of ice fabrics modelling spanning the microscale to the macroscale

There are currently several approaches for modelling ice fabrics. Some approaches model The effects of deformation on the dynamics of ice covers a vast range of scales from the order of microns for studying grain-grain interactions, to continental scales of 1000s of kilometres when studying ice-sheets. Consequently, different approaches must be used depending on the scale one seeks to work on, with microscale models serving to provide parametrisations of small-scale processes for use in larger scale models. At the scale of micrometres and millimetres, there exist several approaches for modelling the microstructure directly (Llorens et al., 2016; Kennedy and Pettit, 2015)(e.g. Llorens et al., 2016; Kennedy and Pettit, 2015). This involves simulating grain-grain interactions and imposes deformation as a boundary condition with deformation regimes imposed via stress or velocity boundary conditions at the edges of the numerical domain. This is useful for improving our understanding of ice microstructure and fabric evolution but is numerically expensive. At the other end of the scale, models such as presented by Gillet-Chaulet et al. (2005) . However, it cannot be scaled-up to be incorporated into ice-sheet model due to the numerical cost. At the largest scale, ice-sheet models typically neglect the effect of fabric entirely. The state-of-the-art for incorporating fabric evolution into large-scale models is to track the evolution of tensorial descriptions of the fabric, without including migration recrystallization. These cannot accurately reproduce detailed fabric patterns but are computationally cheap enough for integration into large-scale models (Gagliardini et al., 2013) a 2nd-rank tensor representing the second moment of the orientation density function (to be defined below in Eq. (2)). A key omission in utilising the second moment alone is that it cannot incorporate the important process of migration recrystallization (Gillet-Chaulet et al., 2006; Gagliardini et al., 2013), which is key in terms of producing the details of differing fabric patterns.

Placidi et al. (2010) developed In this paper, we use the SpecCAF model from Richards et al. (2021), which forms a continuum model including all relevant processes (see section 2.1.1). This was recently accurately solved using a spectral method and constrained against experiments by Richards et al. (2021) of the full orientation density function with parameterisations of the underlying processes calibrated using laboratory experiments. In the hierarchy of ice modelling, SpecCAF seeks to model ice fabrics at a larger scale than models by Llorens et al. (2017) for example. SpecCAF acts as a continuum model for fabric evolution which, through use of a spectral method, is sufficiently efficient computationally that it can be incorporated into ice-sheet models, while retaining all key processes. In this continuum approach, grain-to-grain interactions are incorporated statistically through parameterisations of an orientation density function representing a distribution function of c -axes averaged over a polycrystal. The model thereby describes the evolution of the orientation density function. Since it incorporates parameterisations of the mean effect of grain-grain interactions, there is no need to represent the strain and stress fields explicitly within the

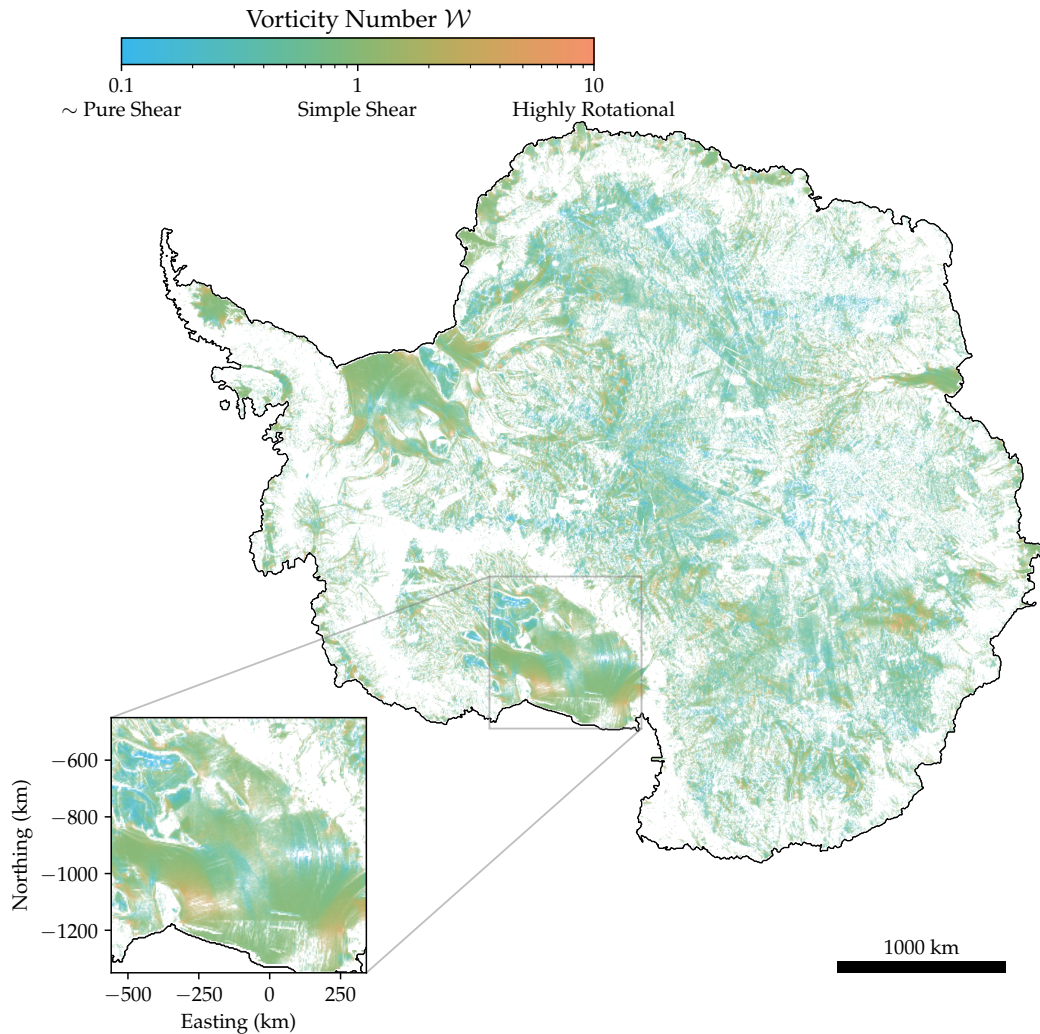


Figure 5. Vorticity number (defined in Eq. (1)) calculated from the surface velocity data of Antarctica (Mouginot et al., 2019) after averaging over a 10×10 block and taking the mean value within each block. The calculation uses the horizontal velocity fields from the observed surface velocity combined with an estimate of the average vertical shear predicted to occur in the top 25% of the ice sheet using the shallow-ice-approximation. The colour shows the vorticity number on a log scale. The transparency shows the relative error: an error in \mathcal{W} of 100% or greater is plotted as white and an error of 0% is plotted as the full colour. The inset shows the Ross Ice Shelf, with the easting and northing in Antarctic polar stereographic coordinates. This figure shows considerable variation in vorticity number across the continent, including deformation regimes not accessible in the laboratory (this result is also highlighted in Fig.??).

230 microstructure. However, these interactions are incorporated statistically within the model by parameterisations of the net effect of these interactions calibrated using laboratory experiments. This model (SpecCAF) has been shown to predict fabrics accurately with only temperature and deformation in both the endmember limits of compression and simple shear. The model can

predict fabric evolution with only the velocity gradient and temperature as inputs. SpecCAF reproduces fabrics from experiments performed in compression and simple shear.

235 We note that, by itself, SpecCAF models fabric evolution only, it does not include a viscosity formulation like the CAFFE model of Placidi et al. (2010). Thus, we take the velocity gradient as being prescribed, and consider the evolution of fabrics that occur as a result. In principle, the model could be coupled to a flow law (viscosity formulation) describing the effect of the fabric on the anisotropy. This could be considered in future.

2.4 Open questions addressed here

In this paper we use the SpecCAF model to address several open questions. First, we the open questions highlighted in the introduction: 240 what fabrics are produced under any given (incompressible) two-dimensional deformation regime, how do fabrics evolve at the very high strains, what strains are necessary to reach steady state, and how are these final steady states dependent on the parameters?

In section 3 we review the SpecCAF model and clarify its underlying modelling assumptions and comparison with other modelling approaches. In section 4.1 we determine for the first time the evolution of fabrics in general 2D de- 245 formations deformation regimes, bridging the complete spectrum from pure shear to rigid-body rotation, across the range of temperatures seen in ice sheets. We explore how fabric patterns evolve, and In section 4.2 we construct a complete regime diagram for two-dimensional deformation regimes documenting fabrics that arise over the space of temperature, deformation regime, and strain, and explain the physical balances leading to these fabrics. Finally, we present a complete assessment of in section 4.3 we investigate the time or strain scales over which ice fabric evolution takes place, as well as investigating the steady-state 250 properties strength of ice fabrics, such as fabric strength and finite strain required to reach steady state, across the space of deformation regime and temperature. We then discuss the implication of these results for the interpretation of ice cores (section 5.3) and ice flow (sec 5.4).

3 Methods

3.1 The continuum approach

255 The SpecCAF model, following work by Placidi et al. (2010), model described in this section is based on Placidi et al. (2010) has already been described in Richards et al. (2021). For the sake of clarity we include an explanation here as well. The SpecCAF model uses a continuum approach to represent the mass distribution of c -axes within a polycrystal $\rho^*(\mathbf{x}, t, \mathbf{n})$, termed the orientation mass density, defined according to

$$\rho(\mathbf{x}, t) = \int_{S^2} \rho^*(\mathbf{x}, t, \mathbf{n}) d\mathbf{n}, \quad (2)$$

260 In this equation $\rho^* d\mathbf{n}$ where $\rho(\mathbf{x}, t)$ is the mass density of ice, and \mathbf{n} is a unit vector representing the direction of a c -axis. Here, $\rho^*(\mathbf{x}, t, \mathbf{n}) d\mathbf{n}$ is the mass fraction of grains with orientations towards the unit orientation vector directed towards \mathbf{n} within the solid

angle $d\mathbf{n}$. Therefore, in accordance with the equation above, integrating ρ^* over the space of possible orientations (the surface of a unit sphere S^2) gives the mass density of ice at that particular point in physical space. The unit vector \mathbf{n} is defined by two angles in spherical coordinates $\mathbf{n}(\theta, \varphi)$, representing any possible orientation. As we are modelling orientation evolution, the gradient operator is restricted so only the two angles θ, φ (and not the length of the vector) change in spherical coordinates:

$$\nabla^* \mathbf{a}^* = \frac{\partial \mathbf{a}^*}{\partial \mathbf{n}} - \left(\frac{\partial \mathbf{a}^*}{\partial \mathbf{n}} \cdot \mathbf{n} \right) \mathbf{n} = \frac{\partial a_i^*}{\partial n_j} - \frac{\partial a_i^*}{\partial n_l} n_l n_j,$$

where \mathbf{a}^* is an arbitrary vector in orientation space, $\rho(\mathbf{x}, t)$.

We model the evolution of the orientation mass density. SpecCAF incorporates the effect of basal-slip deformation, migration recrystallization and rotation recrystallization (all as functions of temperature), as well as rigid-body rotation, to develop an evolution equation for the orientation mass density ρ^* . As discussed above, the model evolves ρ^* defined in Eq. under the effects of vorticity, basal-slip deformation, rotational and migration recrystallization, using the model as the dependent variable, with the net effects of grain-to-grain interactions incorporated through parametrisations. This is similar to other continuum approaches, for example how explicit descriptions of particle interactions are not included in the Stokes equations, yet are satisfactorily modelled statistically through parameterisation in the form of a constitutive relation. In the present case, rotation recrystallization is modelled as a diffusion of concentrations of ρ^* , originally the idea of Gödert (2003). Migration recrystallization is modelled through an orientation dependent source-term producing ρ^* preferentially at orientations where grains would be likely to have a large basal shear-stress, and vice-versa. Basal-slip deformation is incorporated in accordance with the ‘deck-of-cards’ analogy, and assuming linear dependence on the strain-rate tensor (Placidi et al., 2010). The resulting continuum model has been shown to reproduce all detailed features of the distribution functions calculated from experimental samples (Richards et al., 2021).

The essential continuum approach was proposed previously by Faria (2001, 2006). Grains with the same orientations are called a *species*. There has been discussion in the literature (Gagliardini, 2008; Faria et al., 2008) on whether this theory implicitly includes a *Taylor assumption*, namely, that all ice grains forming the polycrystal experience the same strain-rate. The Taylor assumption has been shown not to be valid for ice (Castelnaud et al., 1998). To summarise this debate, Gagliardini (2008) suggests that the assumption in Faria (2006) that the strain-rate of a species is independent of orientation is equivalent to every grain undergoing the same deformation (a Taylor assumption). However, Faria et al. (2008) rejected this assertion and replied that this assumption only requires that grains move with the surrounding material, with no direct constraint on the individual deformation of grains. In accordance with the continuum approach, the net effect of deformations on individual grains, which can vary from grain to grain, is incorporated via parametrisations of the overall net effect of these interactions. Since these parametrisations are calibrated using fully resolved experiments (Richards et al., 2021), they represent net effects relevant to real samples in which grains do not all experience the same strain. Therefore, the continuum model does not impose a Taylor assumption on the grain deformation. Furthermore, care should be taken in attributing our calibrated parameters as applying specifically to grain-grain interactions rather than the bulk interactions representing their net statistical effects in the model.

295 Despite the model not including the Taylor hypothesis, the term for basal-slip deformation in the equation below is similar to that which would be derived from a Taylor homogenisation of ice under a simple basal-slip only model (Gagliardini et al., 2009). The only exception is that the rate of viscoplastic deformation can vary relative to rigid-body rotation.

3.2 Model specification

The evolution equation for ρ^* under the framework described above was first defined in Placidi et al. (2010):

$$300 \quad \frac{\partial \rho^*}{\partial t} = -\nabla^* \cdot (\rho^* \mathbf{v}^*) + \lambda \nabla^{*2}(\rho^*) + \beta (\mathcal{D}^* - \langle \mathcal{D}^* \rangle) \rho^*, \quad (3)$$

The term where λ and β are parameters, to be defined below. Here, ∇^* is the gradient operator in orientation space defined by:

$$\nabla^* \mathbf{v}^* = \frac{\partial \mathbf{v}^*}{\partial \mathbf{n}} - \left(\frac{\partial \mathbf{v}^*}{\partial \mathbf{n}} \cdot \mathbf{n} \right) \mathbf{n} = \frac{\partial v_i^*}{\partial n_j} - \frac{\partial v_i^*}{\partial n_l} n_l n_j, \quad (4)$$

305 which is the gradient operator restricted to the surface of a sphere. The parameters λ and β represent the rates of rotational recrystallization and grain-boundary migration, respectively. The orientationally dependent term \mathcal{D}^* will be defined below in Eq. (6). The term \mathbf{v}^* is defines the orientation transition rate, defined as: by Placidi et al. (2010) as:

$$v_i^* = W_{ij} n_j - \iota (D_{ij} n_j - n_i n_j n_k D_{jk}). \quad (5)$$

The term $W_{ij} n_j$ in Eq. (5) represents the effect of vorticity on the CPO. The second term models basal-slip deformation. The non-dimensional parameter ι represents the ratio of basal-slip deformation to rigid-body rotation. Equation was first used to describe the rotation of an individual ice grain (Svendsen and Hutter, 1996) but here it is used to describe a continuum. We refer the interested reader to Richards et al. (2021) for more details.

315 The term $\nabla^{*2}(\rho^*)$ models rotational recrystallization through parameter λ (s^{-1}) represents the rate of rotational recrystallization, which can be modelled by a diffusion in orientation space (Gödert, 2003). The rate is controlled by the parameter λ Migration recrystallization is modelled by an orientation-dependent source term, with the rate controlled by β (s^{-1}). Migration recrystallization is modelled by the term $(\mathcal{D}^* - \langle \mathcal{D}^* \rangle) \rho^*$, which acts as an orientationally dependent source term. The deformability \mathcal{D}^* is defined as The orientation dependence is governed by the deformability, defined by:

$$\mathcal{D}^* = 5 \frac{(D_{ij} n_j)(D_{ik} n_k) - (D_{ij} n_j n_i)^2}{D_{mn} D_{nm}}. \quad (6)$$

320 The parameter β (s^{-1}) controls the rate of migration modelled Placidi et al. (2010) give the physical interpretation of \mathcal{D}^* as the (normalised) square of the shear strain rate resolved onto the basal plane. Because ice deforms primarily by basal slip, the resolved shear rate on the basal plane also drives the accumulation of deformation energy in the physical grain, which drives migration recrystallization. The average of \mathcal{D}^* is defined as:

$$\langle \mathcal{D}^* \rangle = \int_{S^2} \frac{\rho^*}{\rho} \mathcal{D}^* \, d\mathbf{n} \quad (7)$$

At a given orientation \mathbf{n} , if $\mathcal{D}^* > \langle \mathcal{D}^* \rangle$ then $\rho^*(\mathbf{n})$ will increase. This models If \mathcal{D}^* is greater than the average value $\langle \mathcal{D}^* \rangle$ then \mathcal{D}^* at that orientation will increase, as implied by the final term on the right hand side of Eq. (3). This corresponds to grains growing

or nucleating at this orientation due to migration recrystallization. This source term always conserves the integral of ρ^* over orientation space with this orientation.

325 Note that the total production and consumption of \mathcal{D}^* always balance. The factor of 5 in Eq. (6) is a convention. The reader is referred to Placidi et al. (2010) or Richards et al. (2021) for a more detailed explanation.

3.3 Non-dimensionalisation

To apply Eq. (3) to spatially homogeneous fabrics and to compare to fabrics deformed in the laboratory we perform a non-dimensionalisation as in Richards et al. (2021), where we non-dimensionalise by a characteristic density ρ_0 and strain-rate, which we

330 define as:

$$\dot{\gamma} = \sqrt{\frac{1}{2} D_{ij} D_{ji}}. \quad (8)$$

This is the effective strain-rate $\dot{\gamma}$. We represent , corresponding to the second-invariant of the strain-rate tensor \mathbf{D} . The strain-rate we non-dimensionalise with in this paper is half the strain-rate we used in Richards et al. (2021), which was based on the experimental strain-rate. The non-dimensional variables are represented with tildes and they are defined as:

$$335 \quad \tilde{\rho}^* = \frac{\rho^*}{\rho_0}, \quad \tilde{\mathbf{D}} = \frac{\mathbf{D}}{\dot{\gamma}}, \quad \tilde{\mathbf{W}} = \frac{\mathbf{W}}{\dot{\gamma}}$$

$$\tilde{\lambda}(T, \dot{\gamma}) = \frac{\lambda(T, \dot{\gamma})}{\dot{\gamma}}, \quad \tilde{\beta}(T, \dot{\gamma}) = \frac{\beta(T, \dot{\gamma})}{\dot{\gamma}}.$$

As in Richards et al. (2021) this gives the non-dimensional form of Recasting Eq. (3) in terms of the non-dimensional variables above, we obtain:

$$\frac{\partial \tilde{\rho}^*}{\partial t} = -\nabla^* \cdot [\tilde{\rho}^* \tilde{\mathbf{v}}^*] + \tilde{\lambda} \nabla^{*2}(\tilde{\rho}^*) + \tilde{\rho}^* \tilde{\beta}(\mathcal{D}^* - \langle \mathcal{D}^* \rangle), \quad (9)$$

340 where

$$\tilde{v}_i^* = \tilde{W}_{ij} n_j - \iota (\tilde{D}_{ij} n_j - n_i n_j n_k \tilde{D}_{jk}).$$

is the non-dimensional form of the orientation transition rate (Eq. (5)). Richards et al. (2021) constrained the non-dimensional parameters $\tilde{\lambda}, \iota, \tilde{\beta}$ as functions of temperature. The parameters are constrained as :

$$\tilde{\lambda} = 3.04 \times 10^{-4} T + 0.161$$

$$\iota = 0.0259 T + 1.78$$

$$\tilde{\beta} = 0.171 T + 5.90$$

345 where T is in °C. Equations This was done by finding the parameters which gave a best fit to experimental results in simple shear. These parameters were then found to predict well fabric produced in the other endmember deformation regime of (unconfined) compression. In this paper, we use a best fit from the entire inversion performed in Richards et al. (2021), rather than just from the inversion performed in simple shear. Furthermore, as the strain-rate we use to non-dimensionalise is half that used in Richards et al. (2021), the non-dimensional recrystallization parameters ($\tilde{\lambda}, \tilde{\beta}$) used

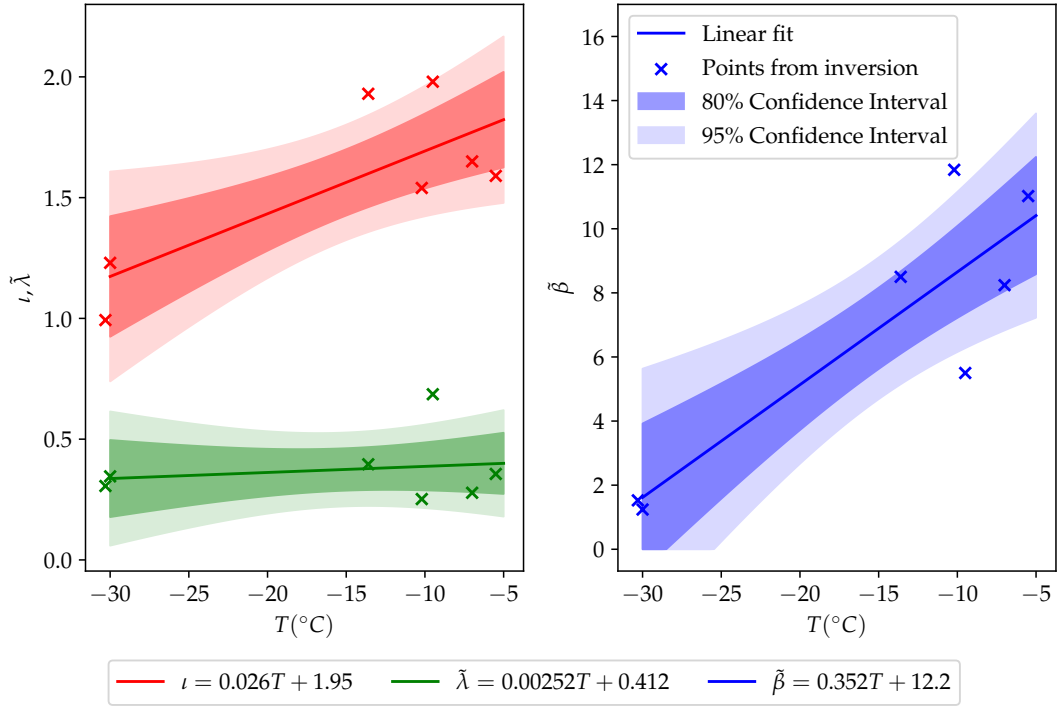


Figure 6. The model parameters $\iota, \tilde{\lambda}, \tilde{\beta}$ as functions of temperature, determined by linear regression to experimental data in both compression and simple shear, as conducted in Richards et al. (2021). The 95% and 80% confidence intervals are shown.

350 in this paper are double those used in Richards et al. (2021). The true parameters (λ, β) are unchanged. The non-dimensional parameters as functions of temperature are shown in Fig. 6, along with the data points used in the inversion from Richards et al. (2021) and 80% and 95% confidence intervals. In the accompanying supplement to this article a parameter sensitivity study can be found, reproducing the figures below with (a) $\iota_{\max}, \tilde{\beta}_{\max}, \tilde{\lambda}_{\min}$ and (b) $\iota_{\min}, \tilde{\beta}_{\min}, \tilde{\lambda}_{\max}$, with the max and min values taken from the 80% confidence interval in Fig. 6. (a) and (b) are chosen to give the strongest and weakest fabric respectively.

355 and weakest fabric respectively.

Equation (9) and the parameters defined by the best fit lines in Fig. 6 combined, when solved with the spectral method defined in Richards et al. (2021), represent the SpecCAF model.

3.4 Pole figure and cross section representation

To illustrate As a preliminary illustration of the model output and its representation, we show in Fig. 7 an example of model output obtained by solving the model at $T = -5^{\circ}\text{C}$ $T = -5^{\circ}\text{C}$, in simple shear ($\mathcal{W} = 1$). The principal axes are orientated at $\theta = \pm 45^{\circ}$ directions of the pole figure. To visualise how the fabric changes with increasing strain, we plot slices of the pole figure at $y = 0$. The example pole figure in (a) is plotted at a strain of $\gamma = 0.5$ $\gamma = 0.345$. The value of ρ^* at $y = 0$ is plotted in

360 output obtained by solving the model at $T = -5^{\circ}\text{C}$ $T = -5^{\circ}\text{C}$, in simple shear ($\mathcal{W} = 1$). The principal axes are orientated at $\theta = \pm 45^{\circ}$ directions of the pole figure. To visualise how the fabric changes with increasing strain, we plot slices of the pole figure at $y = 0$. The example pole figure in (a) is plotted at a strain of $\gamma = 0.5$ $\gamma = 0.345$. The value of ρ^* at $y = 0$ is plotted in

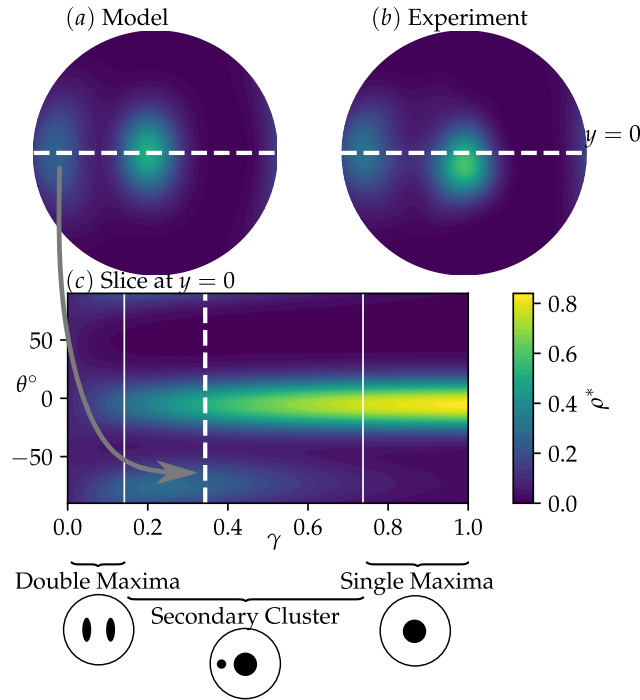


Figure 7. To illustrate the fabric we show a simulation in simple shear at $T = -5^\circ \text{C}$. (a) shows a pole figure from the model at $y = 0.5$ an effective strain of $\gamma = 0.345$ (where the strain-rate is defined as in Eq. (8)). (b) shows a pole figure from laboratory experiments (Qi et al., 2019) at the same temperature and strain, showing good agreement. More comparisons like this can be found in Richards et al. (2021). The white dotted line in (a) and (b) shows $y = 0$. (c) shows ρ^* at $y = 0$ against strain. Here the white dotted line highlights the strain at which the pole figure is plotted. θ is the polar angle. Also highlighted is the classification of the different fabric types at different strains; from double-maxima to secondary cluster to the steady state single maxima. For this figure only the principal axes of deformation are oriented at $\theta = \pm 45^\circ$.

(c) for each strain. This shows how the CPO develops from an isotropic fabric. A secondary cluster can clearly be seen as a transient feature which has mostly disappeared by $\gamma = 0.8$.

365 As an example comparison of the model prediction and experimental observations, we have included a pole figure from laboratory experiments (Qi et al., 2019) in Fig. 8b. This is at the same temperature and strain as the model output in (a). There is very good agreement between the model and experiments. More experimental comparisons are detailed in Richards et al. (2021), showing that the model is able to generally capture both qualitative and quantitative features of fabrics observed in existing experiments.

4.1 General fabric evolution: dependence on temperature and vorticity number

We explore fabric evolution across a complete, **continuous** range of vorticity numbers \mathcal{W} **and for two-dimensional deformation regimes** (spanning $\mathcal{W} = 0$ to ∞), **and a continuous range of temperatures** T relevant to ice-sheet flow ($T = -30$ to -5 ° C). **For all cases, we assume an initially isotropic fabric.** To make comparisons, we will limit our analysis to fabrics undergoing a constant two-dimensional deformation and at a constant temperature. The vorticity number, defined in Eq. (1), gives the ratio of vorticity to strain-rate magnitude. However, it does not fully constrain the velocity gradient. **We To do so, we** define the non-dimensional velocity gradient as:

$$\nabla \tilde{\mathbf{u}} = \frac{\sqrt{2}}{2} \begin{bmatrix} 1 & \mathcal{W} \\ -\mathcal{W} & -1 \end{bmatrix} \quad (10)$$

This gives pure shear for $\mathcal{W} = 0$, simple shear for $\mathcal{W} = 1$ and rigid-body rotation as $\mathcal{W} \rightarrow \infty$. **and keeps the The** principal-axes of the strain-rate tensor $\tilde{\mathbf{D}}$ unchanged. **Furthermore the pre-factor is chosen so the non-dimensional equivalent of the effective strain-rate is kept at unity:**

$$\sqrt{D_{ij}D_{ij}} = 1.$$

deformation are aligned with the coordinate axes and are unchanged as \mathcal{W} varies.

With the velocity gradient fully defined, we explore the fabric dynamics produced across T - \mathcal{W} space in Fig. 8. For each square we show the slice through the pole figure at $y = 0$ (explained in Fig. 7) up to a finite strain of $\gamma = 2\gamma = 1$. The temperature range is from -30 ° C to -10 ° C **-30 ° C to -10 ° C**, temperatures typical in ice sheets (Duval et al., 2010). The vorticity number ranges from $\mathcal{W} = 0.1$, very close to pure shear, and $\mathcal{W} = 10$ representing highly vortical flow with curved streamlines. This provides a detailed picture of how the fabric evolves with increasing strain, providing insights into **deformations deformation regimes** between compression and simple shear as well analysis of fabrics produced by **deformations deformation regimes** more rotational than simple shear. For low vorticity numbers, a single maximum can be seen at low temperatures which develops into double-maxima as strain increases. As \mathcal{W} increases the clusters are moved by the rotational component of the deformation, resulting in a primary and secondary cluster. The weaker, secondary cluster is gradually consumed by migration recrystallization as strain increases, leading to a single maximum at high strains, for $\mathcal{W} \sim O(1)$.

We **present also show** in Fig. 8 analysis of fabrics produced in highly rotational ($\mathcal{W} > 1$) **deformations deformation regimes**, which as we have shown are prevalent in real-world conditions (**figs. 5,??Figs. 4,5**). Figure 8 shows that the fabric is strongest for $\mathcal{W} = 1$, and weakens as vorticity increases past this. For example, for $\mathcal{W} = 10$ there is only a very weak CPO produced. **Furthermore at high , at large** vorticity numbers oscillation can be seen in the fabric pattern. **Figs. S1 and S2 in the supplement show that variations in the parameters from Fig. 6 affect the strength of the primary cluster primarily, but do not affect the variation with vorticity number or the transition from one fabric type to another.** To further analyse **very high** the limit of very large vorticity numbers we show the fabric produced as $\mathcal{W} \rightarrow \infty$ in Fig. 9. This fabric is seen for any vorticity number above

400 $\mathcal{W} \approx 50$. To measure fabric concentration the J index is often used (Bunge, 1982), defined as:

$$J = \int_{S^2} \tilde{\rho}^{*2} dn. \quad (11)$$

The J index of this fabric is 1.121.16, very close to completely isotropic ($J = 1$). It is unlikely this weak girdle fabric would be distinguishable from an isotropic fabric in a physical sample, where the CPO is determined by sampling a limited number of grain orientations.

405 4.2 Fabric regime diagrams for cluster angle and fabric type

To distil all the complex information shown in Fig. 8 and make this information more easily accessible, we analyse both the presents results showing the variation of the angle of the primary cluster and the regimes of different fabric patterns across the $\mathcal{W}-T$ space. The angle between the primary cluster and the compression axis closest principal axis of deformation (i.e. the axis of compression) is shown in Fig. 10 at six separate finite strain values, across $\mathcal{W}-T$ space. Even at a low finite strain of $\gamma = 0.3$ there is already an established difference in angle across the parameter space (Fig. 10a). Low temperatures and low vorticity numbers have the primary cluster most closely aligned with the compression axis. The angle then increases as both temperature and especially vorticity number increase. As strain increases the variation in angle increases. However, for a finite strain greater than 1.0.5 the angle is mostly invariant with strain. Across the strain and temperature range, an angle of around 40° implies simple shear ($\mathcal{W} \approx 1$), whereas if the primary cluster and compression axis are coincident, this suggests pure shear at $T \approx -30^\circ\text{C}$ $T \approx -30^\circ\text{C}$.

Figures S3 and S4 in the supplement show Fig. 10 with the strongest and weakest possible fabric based on the 80% confidence intervals in Fig. 6. At low vorticity numbers and temperatures, the angle between the primary cluster and compression axis is slightly sensitive to variations in parameters, but outside of this space the angle is roughly unchanged.

420 As a means to visualise the variety of fabrics in terms of both the parameter space and across possible finite strains we show a regime diagram for fabric patterns in Fig. 11. To define whether a fabric is a double-maxima, secondary cluster or single-maxima we take the ratio of the two largest peaks in the fabric. If the 2nd largest peak is less than 10% the strength of the largest peak, it is defined defines as a single-maxima. If the strength of the 2nd largest peak is between 10% and 90% of the largest peak, it is defined as a secondary cluster. If it is $> 90\%$ it is defined as a double-maxima. Contour lines of primary cluster angle at 20° and 50° are also shown. This shows the different fabric types (Fig. 1) across the space of temperature, vorticity number and finite strain. The figure is in the same format as 10.

Figure 11a shows the initial fabric after a finite strain of only $\gamma = 0.3$. There are three regimes at this finite strain. For approximately $\mathcal{W} < 1$ $\mathcal{W} < 0.7$ a double-maxima is produced. There is a small region, at high vorticity numbers and primarily at low temperatures but extending into high temperatures, at which a single-maxima is produced. Otherwise a secondary cluster is produced, this occurs for relatively high vorticity numbers and is more dominant at higher temperatures, as expected. At higher finite strain the double-maxima pattern becomes less prevalent, only occurring at lower vorticity numbers or not at all. This highlights the transient nature of this pattern. As a reminder, the double-maxima is the 2D equivalent of a cone-

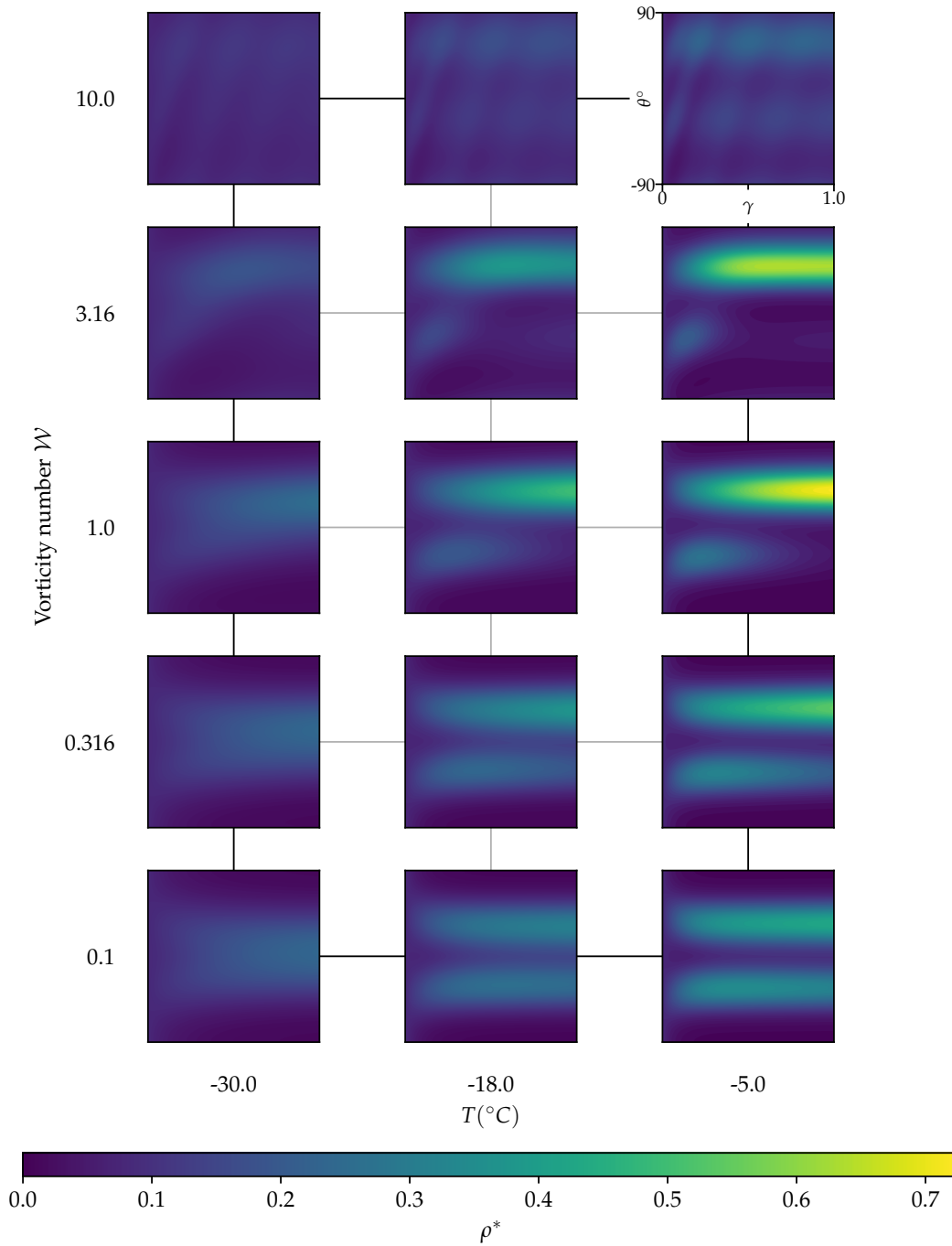


Figure 8. Slices of the pole figure showing the value of ρ^* at $y = 0$ for an array of temperatures and vorticity numbers. All $y = 0$ plots go to a strain of $\gamma = 2\gamma = 1$. The colour limits are the same for all plots.

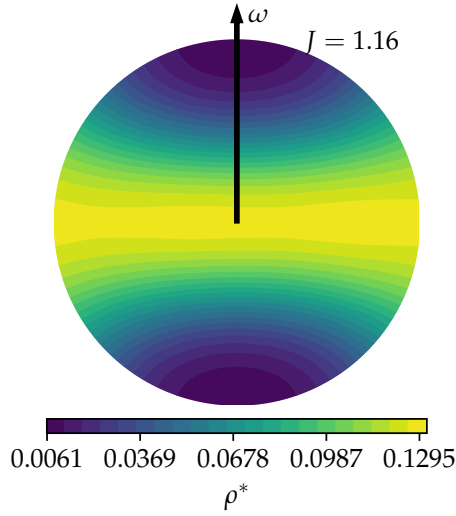


Figure 9. Pole figure for $\mathcal{W} \rightarrow \infty$ and $T = -5^\circ\text{C}$ at steady-state. A very weak girdle fabric is produced, with the girdle coincident with the axis of vorticity, shown. This CPO has a J index of 1.16, where $J = 1$ is an isotropic fabric.

shape fabric (Fig. 1). The double-maxima fabric is only present up to a finite strain of about $\gamma = 0.5$. In Fig. 11c, at $\gamma = 1.0$ the parameters space is dominated by single-maxima and secondary cluster patterns. Ice fabrics which develop at higher
 435 temperatures $T > -20^\circ\text{C}$ are dominated by secondary cluster patterns, with the exception of around $\mathcal{W} \approx 3$, where a single-maxima occurs as because the secondary cluster is too weak. At lower temperatures $T < -25^\circ\text{C}$ a single-maxima is produced as because migration recrystallization is not active enough for multiple clusters to be produced. This balance between a single-maximum fabric and a secondary cluster fabric continues as the finite strain increases, with a single-maxima also becoming more prevalent at lower vorticity numbers at the highest finite strains high temperatures for vorticity numbers around 1 (Fig. 11e and f).

440 Figures S5 and S6 in the supplement show Fig. 11 with the strongest and weakest possible fabric based on the 80% confidence intervals in Fig. 6. The overall picture is similar. The variation with vorticity number is approximately unchanged and boundaries between the regimes shift by roughly $\pm 7^\circ\text{C}$.

To illustrate the difference in pole figure patterns at the same finite strain but different temperatures and deformations deformation regimes we plot pole figures at a finite strain of $\gamma = 2$ (Fig. 12) overlaid onto a regime diagram of fabric patterns. The
 445 pole figures are centred at the vorticity number and temperature they are simulated at. Figure 12 highlights fabrics are still variable despite being in the same regime. The fabric at $\mathcal{W} = 1, T = -5^\circ\text{C}$ is much stronger than the fabric at $\mathcal{W} = 10, T = -30^\circ\text{C}$ or $\mathcal{W} = 0.1, T = -30^\circ\text{C}$ or $\mathcal{W} = 10, T = -30^\circ\text{C}$ or $\mathcal{W} = 0.1, T = -30^\circ\text{C}$, however they are all single-maxima. We also note the difference in angle of the primary cluster across the parameter space: approximately 0° for $\mathcal{W} = 0.1, T = -30^\circ\text{C}$ or $\mathcal{W} = 0.1, T = -30^\circ\text{C}$ but increasing as \mathcal{W} and T increase, as shown in Fig. 10.

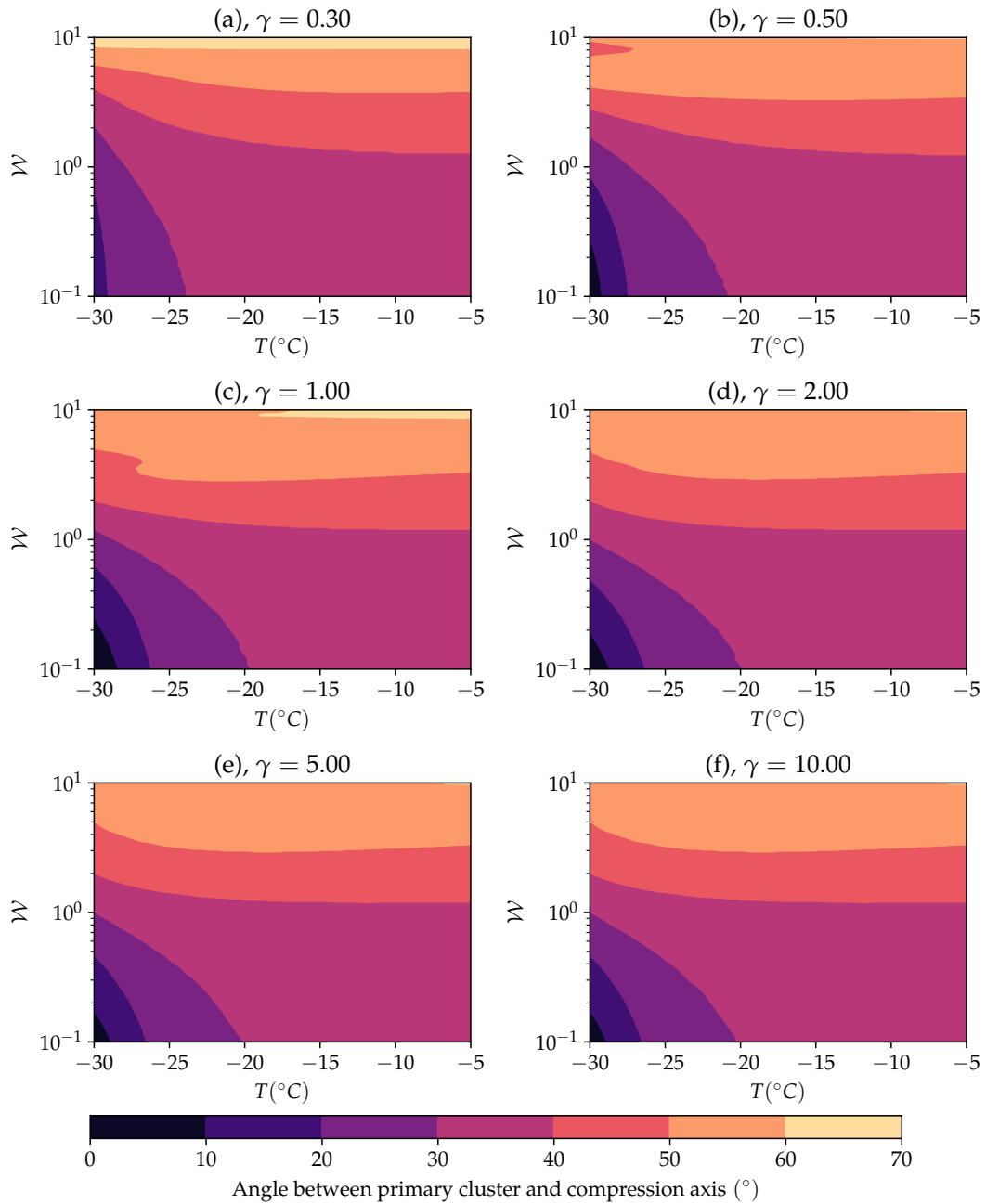


Figure 10. Diagram Contour plots showing the angle (in degrees) of the largest cluster from the compression axis. Panels are shown for progressively increasing finite strain values. This angle is fairly invariant with finite strain. The resolution of this figure is 50×50 across the parameter space.

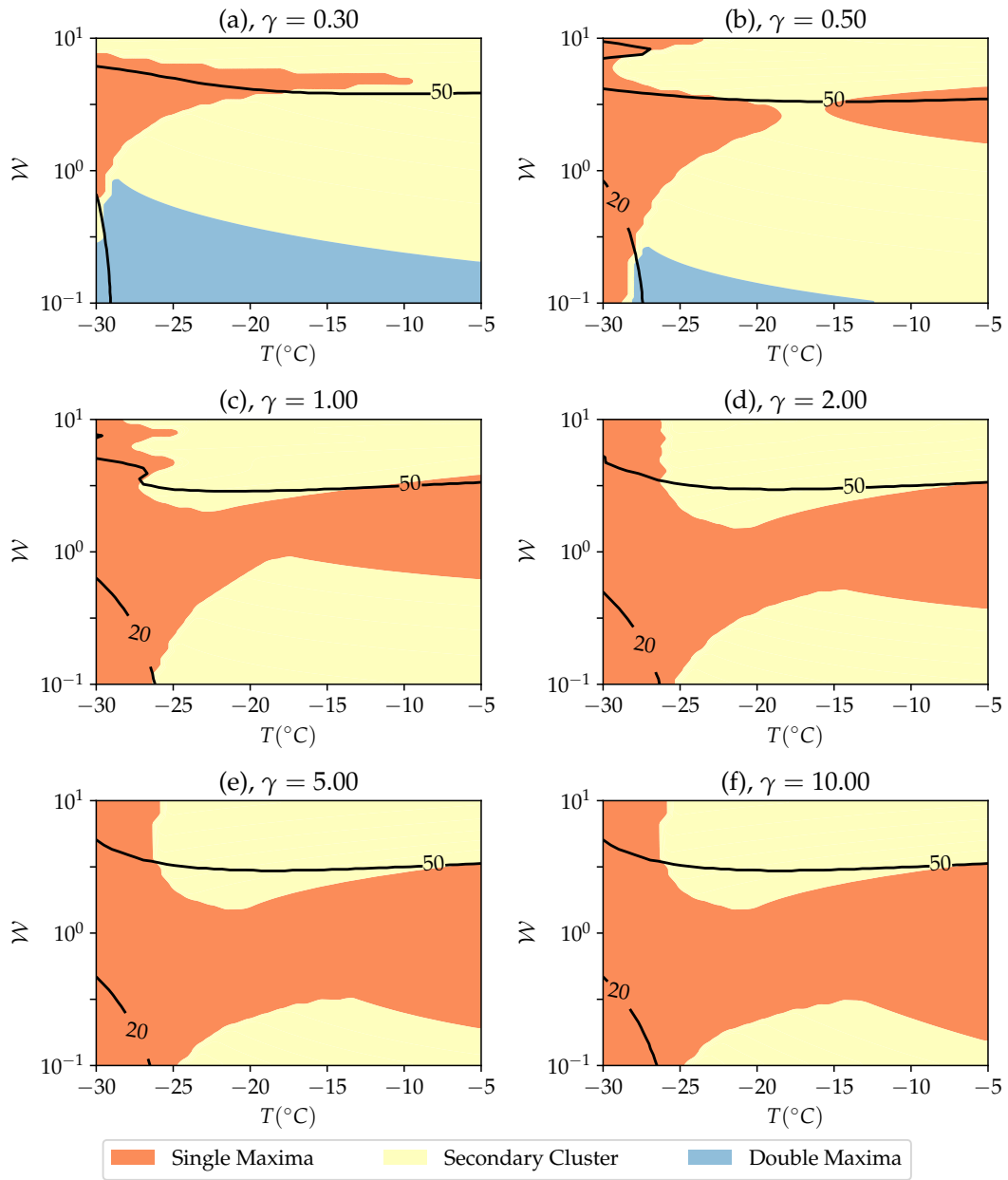


Figure 11. Regime diagram of the different fabric patterns which occur (defined in Fig. 1). The angle of the primary cluster in Fig. 10 at 20° and 50° is also overlaid. As in Fig. 10 diagrams are shown for discrete strain values. [The resolution of this figure is \$50 \times 50\$ across the parameter space.](#)

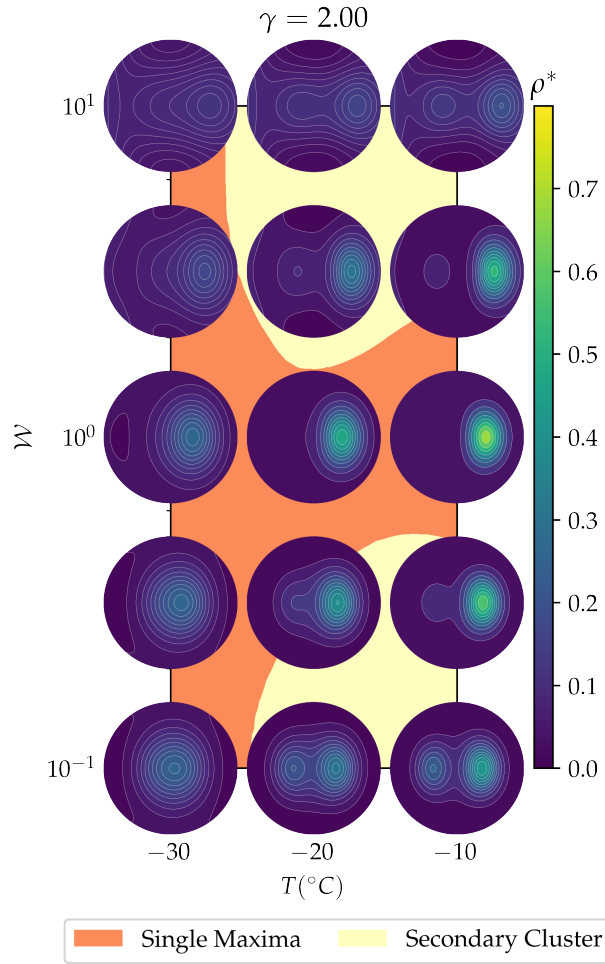


Figure 12. Pole figures overlaid onto the regimes at $\gamma = 2$. The pole figures are centred at the vorticity number and temperature they occur.

450 4.3 Steady state Analysis of fabric evolution timescales

A variable that is central to the interpretation of ice core fabrics is the finite strain at which the fabric can be said to have reached its final steady state. Our predictions for the final steady state properties are shown in Fig. 13, timescale or, equivalently in the non-dimensional problem, the finite strain over which fabric evolution occurs. In Fig. 13 we explore fabric evolution timescales. Fig. 13a shows the finite strain required to reach halfway to steady-state in (a). We also show the J index when the fabric reaches steady state in (b).

455 Both are shown across the space of \mathcal{W} - T . Here, we define the steady state strain as being reached once the rolling average of the J index (Bunge, 1982), a measure of fabric concentration, defined as:

$$J = \int_{S^2} \rho^{*2} d\mathbf{n}.$$

over a finite strain window of 0.5 gets within 10% of the steady-state value. An example showing the evolution of the J index and the finite strain at which it reaches steady state is illustrated in Fig. 13c.

460 Figure 13a shows the finite strain at which steady-state is reached across the T - \mathcal{W} space. At the highest temperatures and at vorticity numbers $\mathcal{W} \approx 0.02$ the highest finite strain is needed to reach a steady-state fabric, of around $\gamma = 14$. This occurs as the very small amount of rotation away from pure shear ($\mathcal{W} = 0$) causes a very slow transition from a double-maxima to a single-maxima, causing the J index to increase. For extremely low vorticity numbers ($\mathcal{W} \approx 0.01$) this change is so gradual that the fabric is defined as 'steady' earlier. Only $\mathcal{W} = 0$ has a stable double-maxima. This switch in J index is halfway to its steady-state strain is not seen at low temperatures as migration recrystallization is not active enough to produce a double-maxima. For all fabrics explored between pure and simple shear ($0 < \mathcal{W} < 1$) a large finite strain is required to reach steady state of $\gamma > 1.3$. Fabrics reach steady state at the lowest finite strains at relatively high vorticity numbers of $\mathcal{W} \approx 4$. At higher vorticity numbers than this there is some oscillation in the fabric causing the J value. This can be considered the half-life over which fabric evolution occurs. Measuring the strain at halfway to steady-state strain to increase. Figure 13b shows the value of J gives insight into the timescale over which fabric development occurs and is more robust measure than estimating the strain at steady-state, which we found was sensitive to parameter variations such as those shown in the supplement. Vorticity numbers closest to 0 and the coldest temperatures have the highest halfway strain. Under these conditions, neither rigid-body rotation nor migration recrystallization are activated to a significant degree: the fabric evolution is dominated by basal-slip deformation. Fabrics also take longer to develop closer to a vorticity number of 0.7, due to the fact that this vorticity number has the strongest fabrics generally. For $\mathcal{W} > 1$ the strain to reach half strength decreases, as the fabrics are shown to be generally weaker as vorticity number increases. This is clearly seen in Fig. 13b (showing the J at the steady state-index a steady-state). Generally, as temperature increases the steady-state fabric always increases in strength. Fabrics are strongest for $\mathcal{W} \approx 0.4$ and at higher temperatures, while for high \mathcal{W} , $J \approx 1$ i. e. an isotropic fabric, as seen at a vorticity number of around 0.7 across almost the whole temperature space.

465

470

475

Figures S9 and S10 in the supplement show Fig. 13 with the strongest and weakest possible fabric based on the 80% confidence intervals in Fig. 8. This figure highlights the effect even a small amount of rotation (i. e. $\mathcal{W} = 0.02$) has on the J value. These figures show that the halfway strain is fairly insensitive to changes in the parameters, with the maximum varying by around $\pm 20\%$. The maximum halfway strain remains at $\mathcal{W} = 0.1, T = -30^\circ \text{C}$ for both Fig. S9 and S10. The J index at steady-state fabric, by making the double-maxima pattern seen in pure shear unstable, is more sensitive to changes in parameters but the general picture of how this variable changes across the T - \mathcal{W} space is similar, with the upper bound showing generally less variation across the parameter space.

480

5 Discussion

485 The analysis we have presented here covers the J index and the finite strain at which it reaches steady state presented here gives predictions for the fabric patterns produced over the whole range of vorticity numbers and temperatures present in the natural world arising for incompressible two-dimensional deformation regimes, a first for fabric modelling. In this paper we We have limited the analysis here to fabrics produced under constant deformation a constant deformation regime and temperature. Although ice in the natural world will undergo changing deformation regimes, our analysis is an important a first step to provide insights into fabrics produced for deformation regimes away from

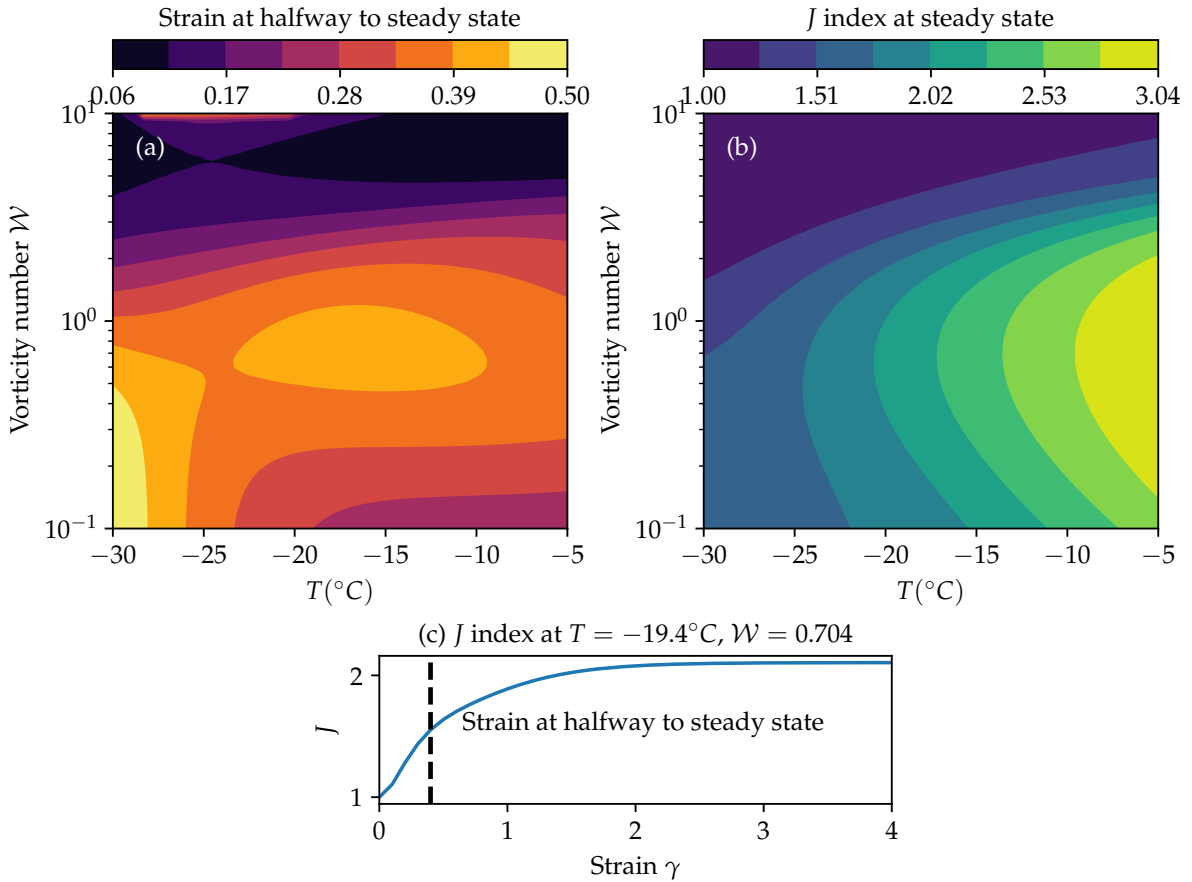


Figure 13. This figure shows information about the Properties of steady-state fabricfabrics across the $\mathcal{W} - T$ parameter space. (a) shows the strain at which the fabric, at constant T and \mathcal{W} , reaches steady-state (defined as a rolling average of the J index over a strain window of 2 gets within 5% of the steady-state value). (b) shows the J index at the steady state. (c) shows the plot of J against strain γ at $T = -30^{\circ}\text{C}$, $\mathcal{W} = 0.01$, with the calculated steady-state strain

490 pure and simple shear. Furthermore, the fabrics analysed here are highly relevant for ice deformed in the laboratory, which is in most cases deformed at constant temperature and vorticity number.

Ice in the real-world will undergo three-dimensional deformations yet it is common to model ice-sheets in two-dimensions along the vertical cross-section, such as in Fig 3. This has been shown to be valid around divides such as in Martín et al. (2009). In some regions, such as ice streams and regions where the ice is floating, the deformation will be more two-dimensional. Nevertheless, exploring general two-dimensional deformations is a good first step away from the isolated, two-dimensional conditions of pure and simple shear alone.

495

5.1 Fabrics Fabric patterns across deformation regime and temperature space

Previous work has focused on modelling fabrics produced at fixed deformations deformation regimes (Llorens et al., 2016), or modelling the deformation experienced by ice at a divide (Bargmann et al., 2012). Due to the computational efficiency of our model, we have been able to perform many thousands of simulations across the parameter space of temperature and vorticity number to show how fabrics vary.

Our work generally shows a smooth transition between these two deformations the two deformation regimes of pure and simple shear, as can be seen in Fig. 8. As shown in Fig. 5 these deformations Such intermediate deformation regimes are important in the real-world (Figs. 3,4,5) and must be taken into account when considering ice fabrics, rather than focusing on the isolated cases of pure and simple shear.

The weak fabric seen for highly rotational flows is novel has not been studied at all so far. This result is interesting as it shows for the first time the fabric produced by highly rotational deformation regimes: a weak girdle fabric. Throughout these deformations deformation regimes we have kept the magnitude of \mathbf{D} , the strain-rate tensor, constant. Therefore, at high vorticity numbers the weak fabric seen in Figs. 8 and 9 is not caused by a lack of deformation. Instead it is due to the rotational component acting to quickly smear any cluster produced by basal-slip deformation or migration recrystallization to orientations where the cluster is consumed by migration recrystallization. The end result as $\mathcal{W} \rightarrow \infty$ is a very weak girdle fabric with the girdle aligned to the axis of vorticity.

The regime diagram in Fig. 11 shows the fabric patterns produced across the space of vorticity number, temperature and strain. From experimentally deformed ice, the vast majority of fabrics produced are cone-shape fabrics (Fan et al., 2020). However, ice deformed in the laboratory in compression can only reach strains of up to $\gamma = 0.5$ and Fig. 11 highlights how double-maxima fabrics are only present up to these strains. Above $\gamma = 0.5$, secondary cluster and single-maxima patterns are more prevalent. Importantly, secondary cluster fabrics, which have been to-date only seen in simple shear ($\mathcal{W} = 1$), can occur at very low vorticity numbers (Fig. 11c,d).

Results from Budd et al. (2013) show a secondary cluster fabric for $W = 0.85, \gamma = 0.34$ and $T = -2^\circ \text{C}$. Extrapolating Fig. 11a would suggest this agrees with our model. Budd et al. (2013) also have another laboratory data point at $\mathcal{W} = 0.52, \gamma = 0.72$ and $T = -2^\circ \text{C}$ which shows a single-maxima pattern. Extrapolating Fig. 11 would predict a secondary-cluster fabric, however close to boundary where the fabric becomes a single-maxima. Furthermore SpecCAF has only been constrained up to $T = -5^\circ \text{C}$, and as ice approaches the melting point the parameters are likely to behave non-linearly, so a simple extrapolation cannot be relied upon.

5.2 Finite strains required to reach steady-state fabrics for fabric evolution

For the interpretation of ice fabrics it is essential that we know the strain at which fabrics reach steady-state timescale (or in the non-dimensional case here, total finite strain) over which fabrics evolve to steady state. In this paper we have presented the first complete assessment of fabric timescales to steady state (Fig. 13), by examining the 'half-life' for fabrics to reach steady-state. In compression, experiments can only reach a maximum effective strain of $\gamma \approx 0.5$. It is often assumed that a strain of around

530 $\gamma = 0.2$ represents a steady state in the mechanical properties, and consequently in fabric (Jacka, 2000). However, recent experiments show that the fabric continues to evolve past this (Piazolo et al., 2013; Qi et al., 2017). It is also known that fabrics require higher finite strain to reach steady-state in simple shear (Journaux et al., 2019). Qi et al. (2017) note that fabric data is required at higher strains than has been achieved to date by compression experiments to link to high-strain natural environments. The results in our paper fill this missing gap. Figure 13 showing the steady-state strain and fabric strength, allows us to quantify when fabrics

535 have reached steady state across the parameter space. The analysis of fabric regimes extends to very high strains of $\gamma = 10$. For low \mathcal{W} , in experiments and in Fig. 8, a CPO quickly develops at very low strain $\gamma \approx 0.2$, (also seen in Craw et al., 2018). Although the fabric pattern does not change as strain increases, it cannot be said to be in steady-state because the concentration of orientation at the clusters continues to increase. It should be noted that any change in fabric intensity will directly affect the mechanical properties such as the degree of viscous and seismic anisotropy (Duval et al., 1983; Matsuoka et al., 2003).

540 Figure 13 shows that between pure and simple shear the strain at which a CPO reaches steady-state, for constant temperature and deformation is very high, always greater than $\gamma = 1.3$. a shows that, for very low temperatures ($T \approx -30^\circ \text{C}$) the strain to reach halfway to steady state is the highest, around $\gamma = 0.5$. as can be seen in Fig. 13c the true steady-state can not be reached to much later as the J index approaches the steady-state value slowly. From this we can make three remarks. Firstly, reaching a true steady state is impossible for experiments performed in compression: finite strains greater than 100% ($\gamma = 1$) are required, higher than what is possible. However reaching steady state for simple shear experiments is possible,

545 especially for ice remark that reaching true steady states at these temperatures in laboratory experiments will be impossible for deformations close to pure shear. Although Fig. 13a shows that, above very low temperatures ($T > -24^\circ \text{C}$), deformation regimes closer to simple shear take longer to reach steady-state. However these strains are more achievable in the laboratory as fabrics can be deformed in torsion such as by Journaux et al. (2019) where finite strains of $\gamma > 3$ (which is required to reach steady-state) are possible. Secondly, the steady-state strain is dependent on deformation and temperature, and varies by more than a factor of four across the space. Thirdly, in terms of steady-state

550 properties, exactly pure shear ($\mathcal{W} = 0$) is a fairly special case: only with no rotational component in the fabric is a double-maxima (or cone-angle) fabric pattern stable as $\gamma \rightarrow \infty$. Deformations in the natural world will always have some rotational component but the majority of fabrics deformed in the laboratory have been deformed in this special case of $\mathcal{W} = 0$, allowing very high strains such as $\gamma > 1.5$ to be reached (Journaux et al., 2019). Furthermore, the strain to reach halfway to steady state is primarily dependent on vorticity number \mathcal{W} , rather than temperature.

5.3 Consequences for ice core interpretation

555 Analysis and interpretation of ice cores remain key for understanding the processes occurring in the natural world, for both understanding the past climate history (Dansgaard et al., 1969) as well as understanding ice sheet dynamics (Faria et al., 2014) (Schytt, 1958). The regime diagrams we have constructed (figs Figs. 10,11) can be used as a toolkit to interpret ice cores. For example a single maxima fabric with an angle of less than 20° between the compression axis and primary cluster centre implies the core has undergone mostly compression at low temperature. If other constraints are available such as knowledge the deformation

560 regime history or temperature has been constant to good approximation, the dominant deformation regime and temperature can be further constrained. As our work here is for constant temperature and vorticity number, any ice core fabric interpretation will inherently assume that an ice core that has been deformed primarily at a dominant temperature and deformation regime over its recent history. Since temperature varies with depth in an ice sheet (Paterson, 1999), this method is likely to be most

reliable for ice cores where the ice is primarily moving horizontally i.e. away far from ice divides. We also assume an initial random orientation for the fabric. Although deformation regime history in the natural world is likely to be complex, this is a reasonable assumption because ice formed from surface accumulation will initially have a random distribution of orientations (Montagnat et al., 2020).

The fabric pattern is a robust way to interpret ice cores, as it requires no assumptions about the deformation regime direction. The regime diagram in Fig. 11 which is based on the fabric pattern only is complex but insights can be drawn nonetheless. For example, the presence of double-maxima fabrics (two equal strength clusters) implies that the fabric has undergone a relatively low strain. A secondary cluster fabric implies that the fabric is likely to be at intermediate strains, and at temperatures $T > -20^{\circ}\text{C}$. A very weak secondary cluster fabric implies a highly rotational deformation regime $W > 3$. Furthermore, we have shown that the presence of a fabric which appears to be isotropic could be indicative not only of no deformation, but also of a highly rotational deformation regimes.

If other information about the fabric history is known, Figs. 10 and 11 can be used in combination to extend this knowledge. For example, if there are independent constraints on the orientation of the deformation regime axis, then the angle of the primary cluster can be used to interpret ice cores as well. As can be seen in Fig. 10 the angle of between the primary cluster and the compression axis is relatively invariant with strain. Knowing this angle can therefore give a good estimate of the vorticity number and temperature, for deformation regimes which are primarily 2D.

5.4 Implications for ice flow properties and modelling

Viscous anisotropy of ice is controlled by the fabric and is a key control of the flow field (e.g. Minchew et al., 2018)(e.g. Alley, 1988). This anisotropy is dependent on the pattern, direction and strength of the fabric. The current approach common in ice-sheet models is to represent anisotropy with an enhancement factor which scales the viscosity, either globally (Graham et al., 2018) or locally (Placidi et al., 2010). The model SpecCAF used in our paper can be coupled with an any anisotropic viscosity formulation to include directional variation in viscosity. This has been done with simplified fabric evolution models which do Martín et al. (2009) has coupled a fabric model to an anisotropic viscosity, but the fabric evolution model used did not include recrystallization and temperature dependence (Martín et al., 2009), which are dominant processes in controlling fabric evolutions and their approach to final steady states, as well as temperature dependence. The high sensitivity of fabric strength and patterns to temperature shown in our paper and in experimental work (Qi et al., 2019) implies the potential for anisotropy to generate may lead to further interesting flow features on top of those caused by anisotropy alone. This can only be captured with a coupled fabric model including a temperature dependent fabric. Temperature can also affect the flow through viscous heating (e.g Hindmarsh, 2004) and a temperature dependent fabric model coupled to anisotropic viscosity such as Gillet-Chaulet et al. (2005) would allow us to understand what proportion of the effects of temperature are a consequence of viscous heating and what proportion arise through temperature induced changes to the fabric.

The fabrics we have shown here give insight into where anisotropy may be most important in an ice sheet. Areas with strong fabrics will be highly anisotropic, with the viscosity varying in different directions. Anisotropic flow is not well studied but initial simulations with coupled anisotropic flow show it can explain hitherto unexplained observations such as syncline patterns

observed under ice divides (Martín et al., 2009). Our analysis of fabrics produced in highly rotational **deformations deformation regimes** showing an almost isotropic fabric (as seen in **figs Figs. 8 and 13b**) implies that in the regions of Antarctica where the flow is highly rotational, which as we can see in Fig. 5 does occur, the fabric will evolve towards a state with limited anisotropy (directional variation in viscosity). However areas of approximately simple shear ($\mathcal{W} = 1$) show the strongest fabrics and hence the strongest effect of anisotropy. **As we have shown in fig ?? this kind of deformation is the most common in Antarctica.** This means viscous anisotropic affects are **expected to be** widespread, further motivating the need to fully represent them in models. In future work it would **also** be possible to explore how seismic wave velocities vary with the different fabrics modelled in this paper, again comparing to real world observations.

6 Conclusions

Prediction of fabric evolution is pivotal for the correct interpretation of ice core fabrics and reliably predicting ice losses in a changing climate using ice sheet modelling. Our work extends the ability to predict fabric evolution from the **end member endmember** deformation regimes of pure and simple shear to general **and rotational flow two-dimensional deformation regimes**. As such the presented study represents **an important a** step towards understanding fabrics in fully general conditions which is key for understanding viscous anisotropy and **therefore large scale ice sheet , in turn, large-scale ice-sheet** flow modelling. We have shown that **deformations deformation regimes** outside of pure and simple shear are important in **natural ice flows such as Antarctica. Furthermore ice flow regimes more rotational than simple shear are not only possible but common in regions such as shear margins and ice streams which are of significant interest (e.g Meyer and Minchew, 2018; ?). common flow scenarios seen in ice-sheets.** There is the potential for future work to extend the modelled fabrics to calculate to seismic anisotropic properties, enabling us to further improve our understanding of ice in natural flows.

The regime diagrams presented are a useful tool to help with the interpretation of ice core data. In combination with other information, such as the plane of deformation **regime** or an estimate of the temperature at which a core was deformed **at**, these regime diagrams can be used to determine the primary deformation **regime** and temperature undergone by an ice core. **We show that for two-dimensional deformations, the double-maxima fabric is not present at high strains when only a small amount of vorticity is present in the deformation regime $\mathcal{W} > 0.1$. This is important as many laboratory experiments are performed for $\mathcal{W} = 0$. Future work could investigate whether this conclusion extends to three-dimensional cone-shape fabrics.**

Highly rotational **deformations deformation regimes** were investigated for the first time and showed a weak girdle fabric aligned to the axis of vorticity. We have also **highlighted how between pure and simple shear true steady states, where both the fabric pattern and fabric intensity are** **unchanging, are only reached at finite strains of at least $\gamma = 1.3$. This could only be achieved in the laboratory by simple shear experiments, such as by Journaux et al. (2019). These strains cannot be achieved in compression experiments. Furthermore the shown how the timescale for fabric evolution, shown by the halfway strain to reach steady-state, changes over the parameter space. Laboratory experiments around simple shear may be able to reach the strains required to get close to steady-state** **properties of pure shear fabrics are different from those with even a very small amount of rotation, however compression experiments, especially at low temperatures cannot achieve the required strains for steady-state.**

The understanding we provide of ice fabrics under a wider range of deformations, which will be seen in the natural world, provides

Our predictions of ice fabric evolution over a wide range of deformation regimes provide insights into how and where viscous anisotropy will be important for ice flow dynamics. Intermediate deformations deformation regimes between pure and simple shear produce the strongest CPOs, suggesting anisotropy will be most important in these regions. Similarly, as highly rotational deformations deformation regimes produce a weak fabric, there is likely to be a less dominant affect of anisotropy in such regions. Our understanding of these issues could be further improved by combining our model with an anisotropic viscosity formulation to model the coupled fully anisotropic flow of ice necessary to predict ice flow in a changing climate.

Code availability. A python implementation of SpecCAF, alongside code to reproduce the figures in the Results section, is available at <http://doi.org/10.5281/zenodo.5607230>

Author contributions. All authors designed the research and edited the manuscript. DR developed the model code, performed the analysis and visualization and wrote the draft.

Competing interests. The authors declare that they have no conflict of interest.

Acknowledgements. This worked was funded by the UK Engineering and Physical Sciences Research Council (EPSRC) grant EP/L01615X/1 for the University of Leeds centre for doctoral training in fluid dynamics.

References

- 645 Alley, R. B.: Fabrics in Polar Ice Sheets: Development and Prediction, *Science*, 240, 493, <https://doi.org/10.1126/science.240.4851.493>, <http://science.sciencemag.org/content/240/4851/493.abstract>, 1988.
- Azuma, N. and Higashi, A.: Mechanical Properties of Dye 3 Greenland Deep Ice Cores, *Annals of Glaciology*, 5, 1–8, <https://doi.org/10.3189/1984AoG5-1-1-8>, <https://www.cambridge.org/core/article/mechanical-properties-of-dye-3-greenland-deep-ice-cores/A8DB954AC8D9C074EA299EF5BBADD9E0>, 1984.
- 650 Bailey, C. M. and Eyster, E. L.: General shear deformation in the Pinaleno Mountains metamorphic core complex, Arizona, *Journal of Structural Geology*, 25, 1883–1892, [https://doi.org/10.1016/S0191-8141\(03\)00044-0](https://doi.org/10.1016/S0191-8141(03)00044-0), <https://www.sciencedirect.com/science/article/pii/S0191814103000440>, 2003.
- Bargmann, S., Seddik, H., and Greve, R.: Computational modeling of flow-induced anisotropy of polar ice for the EDML deep drilling site, Antarctica: The effect of rotation recrystallization and grain boundary migration, *International Journal for Numerical and Analytical*
- 655 *Methods in Geomechanics*, 36, 892–917, <https://doi.org/10.1002/nag.1034>, <https://doi.org/10.1002/nag.1034>, 2012.
- Beam, E. C. and Fisher, D. M.: An estimate of kinematic vorticity from rotated elongate porphyroblasts, *Journal of Structural Geology*, 21, 1553–1559, [https://doi.org/10.1016/S0191-8141\(99\)00110-8](https://doi.org/10.1016/S0191-8141(99)00110-8), <https://www.sciencedirect.com/science/article/pii/S0191814199001108>, 1999.
- Booth, A. D., Christoffersen, P., Schoonman, C., Clarke, A., Hubbard, B., Law, R., Doyle, S. H., Chudley, T. R., and Chalari, A.: Distributed
- 660 Acoustic Sensing of Seismic Properties in a Borehole Drilled on a Fast-Flowing Greenlandic Outlet Glacier, *Geophysical Research Letters*, 47, e2020GL088148, <https://doi.org/10.1029/2020GL088148>, <https://doi.org/10.1029/2020GL088148>, publisher: John Wiley & Sons, Ltd, 2020.
- Budd, W. F., Warner, R. C., Jacka, T., Li, J., and Treverrow, A.: Ice flow relations for stress and strain-rate components from combined shear and compression laboratory experiments, *Journal of Glaciology*, 59, 374–392, <https://doi.org/10.3189/2013JoG12J106>, edition:
- 665 2017/07/10 Publisher: Cambridge University Press, 2013.
- Bunge, H.: *Texture Analysis in Materials Science: Mathematical Models*, Butterworths, London, 1982.
- Castelnaud, O., Shoji, H., Mangeney, A., Milsch, H., Duval, P., Miyamoto, A., Kawada, K., and Watanabe, O.: Anisotropic behavior of GRIP ices and flow in Central Greenland, *Earth and Planetary Science Letters*, 154, 307–322, [https://doi.org/10.1016/S0012-821X\(97\)00193-3](https://doi.org/10.1016/S0012-821X(97)00193-3), <http://www.sciencedirect.com/science/article/pii/S0012821X97001933>, 1998.
- 670 Chauve, T., Montagnat, M., Piazzolo, S., Journaux, B., Wheeler, J., Barou, F., Mainprice, D., and Tommasi, A.: Non-basal dislocations should be accounted for in simulating ice mass flow, *Earth and Planetary Science Letters*, 473, 247–255, <https://doi.org/10.1016/j.epsl.2017.06.020>, <http://www.sciencedirect.com/science/article/pii/S0012821X17303308>, 2017.
- Craw, L., Qi, C., Prior, D. J., Goldsby, D. L., and Kim, D.: Mechanics and microstructure of deformed natural anisotropic ice, *Journal of Structural Geology*, 115, 152–166, <https://doi.org/10.1016/j.jsg.2018.07.014>, <http://www.sciencedirect.com/science/article/pii/S0191814118300646>, 2018.
- 675 Dansgaard, W., Johnsen, S., Møller, J., and Langway Jr., C.: One thousand centuries of climatic record from Camp Century on the Greenland ice sheet, *Science*, 166, 377–381, <https://doi.org/10.1126/science.166.3903.377>, <https://www.scopus.com/inward/record.uri?eid=2-s2.0-0000342638&doi=10.1126%2fscience.166.3903.377&partnerID=40&md5=8fd86cf99a11c9aecf130c0d4be9798d>, 1969.
- Drury, M. and Urai, J.: Deformation-related recrystallization process, *Tectonophysics*, 172, 235–253, [https://doi.org/10.1016/0040-](https://doi.org/10.1016/0040-680)
- 680 1951(90)90033-5, 1990.

- Drury, M., Humphreys, F., and White, S.: Large strain deformation studies using polycrystalline magnesium as a rock analogue. Part II: dynamic recrystallisation mechanisms at high temperatures, *Special Issue Experiments in Solid State Physics Relevant to Lithospheric Dynamics*, 40, 208–222, [https://doi.org/10.1016/0031-9201\(85\)90131-1](https://doi.org/10.1016/0031-9201(85)90131-1), <https://www.sciencedirect.com/science/article/pii/0031920185901311>, 1985.
- 685 Duval, P.: Creep and Fabrics of Polycrystalline Ice Under Shear and Compression, *Journal of Glaciology*, 27, 129–140, <https://doi.org/10.3189/S002214300001128X>, edition: 2017/01/20 Publisher: Cambridge University Press, 1981.
- Duval, P., Ashby, M. F., and Anderman, I.: Rate-controlling processes in the creep of polycrystalline ice, *The Journal of Physical Chemistry*, 87, 4066–4074, <https://doi.org/10.1021/j100244a014>, <https://doi.org/10.1021/j100244a014>, 1983.
- Duval, P., Montagnat, M., Grennerat, F., Weiss, J., Meyssonier, J., and Philip, A.: Creep and plasticity of glacier ice: a material science perspective, *Journal of Glaciology*, 56, 1059–1068, <https://doi.org/10.3189/002214311796406185>, <https://www.cambridge.org/core/article/creep-and-plasticity-of-glacier-ice-a-material-science-perspective/34BA86B28CE3026D0AE8FBF63BFFB54C>, 2010.
- 690 Fan, S., Hager, T., Prior, D. J., Cross, A. J., Goldsby, D. L., Qi, C., Negrini, M., and Wheeler, J.: Temperature and strain controls on ice deformation mechanisms: insights from the microstructures of samples deformed to progressively higher strains at \$-10, \$-20 and \$-30, \$\circ\$, *The Cryosphere Discuss.*, 2020, 1–43, <https://doi.org/10.5194/tc-2020-2>, <https://www.the-cryosphere-discuss.net/tc-2020-2/>, 2020.
- 695 Faria, S.: Mixtures with continuous diversity: general theory and application to polymer solutions, *Continuum Mechanics and Thermodynamics*, 13, 91–120, <https://doi.org/10.1007/s001610100043>, <https://doi.org/10.1007/s001610100043>, 2001.
- Faria, S. H.: Creep and recrystallization of large polycrystalline masses. III. Continuum theory of ice sheets, *Proceedings of the Royal Society A: Mathematical, Physical and Engineering Science*, 462, 2797, <https://doi.org/10.1098/rspa.2006.1698>, <http://rspa.royalsocietypublishing.org/content/462/2073/2797.abstract>, 2006.
- 700 Faria, S. H., Kremer, G. M., and Hutter, K.: Reply to Gagliardini’s comment on ‘Creep and recrystallization of large polycrystalline masses’ by Faria and co-authors, *Proceedings of the Royal Society A: Mathematical, Physical and Engineering Science*, 464, <https://doi.org/10.1098/rspa.2008.0181>, <https://royalsocietypublishing.org/doi/10.1098/rspa.2008.0181>, 2008.
- Faria, S. H., Weikusat, I., and Azuma, N.: The microstructure of polar ice. Part II: State of the art, *Microdynamics of Ice*, 61, 21–49, <https://doi.org/10.1016/j.jsg.2013.11.003>, <http://www.sciencedirect.com/science/article/pii/S0191814113002009>, 2014.
- 705 Fossen, H. and Tikoff, B.: The deformation matrix for simultaneous simple shearing, pure shearing and volume change, and its application to transpression-transension tectonics, *The Geometry of Naturally Deformed Rocks*, 15, 413–422, [https://doi.org/10.1016/0191-8141\(93\)90137-Y](https://doi.org/10.1016/0191-8141(93)90137-Y), <http://www.sciencedirect.com/science/article/pii/019181419390137Y>, 1993.
- Fujita, S., Maeno, H., and Matsuoka, K.: Radio-wave depolarization and scattering within ice sheets: a matrix-based model to link radar and ice-core measurements and its application, *Journal of Glaciology*, 52, 407–424, <https://doi.org/10.3189/172756506781828548>, <https://www.cambridge.org/core/article/radiowave-depolarization-and-scattering-within-ice-sheets-a-matrixbased-model-to-link-radar-and-icecore-measurements-and-its-application/3F55550C441988125BED34BCDD6E2F68>, edition: 2017/09/08 Publisher: Cambridge University Press, 2006.
- Gagliardini, O.: Comment on the papers ‘Creep and recrystallization of large polycrystalline masses’ by Faria and co-authors, *Proceedings of the Royal Society A: Mathematical, Physical and Engineering Sciences*, 464, 289–291, <https://doi.org/10.1098/rspa.2007.0187>, <https://doi.org/10.1098/rspa.2007.0187>, 2008.
- 715 Gagliardini, O., Gillet-Chaulet, F., and Montagnat, M.: A Review of Anisotropic Polar Ice Models: from Crystal to Ice-Sheet Flow Models, *Physics of Ice Core Records II*, 68, <http://citeseerx.ist.psu.edu/viewdoc/download?doi=10.1.1.496.2886&rep=rep1&type=pdf>, 2009.

- Gagliardini, O., Zwinger, T., Gillet-Chaulet, F., Durand, G., Favier, L., de Fleurian, B., Greve, R., Malinen, M., Martín, C., Riva aback, P.,
720 Ruokolainen, J., Sacchetti, M., Schäfer, M., Seddik, H., and Thies, J.: Capabilities and performance of Elmer/Ice, a new-generation ice
sheet model, *Geoscientific Model Development*, 6, 1299–1318, <https://doi.org/10.5194/gmd-6-1299-2013>, 2013.
- Gillet-Chaulet, F., Gagliardini, O., Meyssonier, J., Montagnat, M., and Castelnau, O.: A user-friendly anisotropic flow law for ice-sheet
modeling, *Journal of Glaciology*, 51, 3–14, <https://doi.org/10.3189/172756505781829584>, [https://www.cambridge.org/core/journals/
journal-of-glaciology/article/userfriendly-anisotropic-flow-law-for-icesheet-modeling/09883516ED5805B13E3D2446B3EC0911](https://www.cambridge.org/core/journals/journal-of-glaciology/article/userfriendly-anisotropic-flow-law-for-icesheet-modeling/09883516ED5805B13E3D2446B3EC0911),
725 2005.
- Gillet-Chaulet, F., Gagliardini, O., Meyssonier, J., Zwinger, T., and Ruokolainen, J.: Flow-induced anisotropy in polar ice and related
ice-sheet flow modelling, 2nd Annual European Rheology Conference, 134, 33–43, <https://doi.org/10.1016/j.jnnfm.2005.11.005>, [http://
www.sciencedirect.com/science/article/pii/S0377025705002648](http://www.sciencedirect.com/science/article/pii/S0377025705002648), 2006.
- Gottstein, G. and Shvindlerman, L. S.: *Grain Boundary Migration in Metals: Thermodynamics, Kinetics and Applications*, CRC Press, 1999.
- 730 Gow, A. J.: Deep core studies of the accumulation and densification of snow at Byrd Station and Little America V, Antarctica, CRREL
Research Report, <https://hdl.handle.net/11681/5803>, 1961.
- Graham, F. S., Morlighem, M., Warner, R. C., and Treverrow, A.: Implementing an empirical scalar constitutive relation for ice with flow-
induced polycrystalline anisotropy in large-scale ice sheet models, *The Cryosphere*, 12, 1047–1067, [https://doi.org/10.5194/tc-12-1047-
2018](https://doi.org/10.5194/tc-12-1047-2018), <https://www.the-cryosphere.net/12/1047/2018/>, 2018.
- 735 Gusmeroli, A., Pettit, E. C., Kennedy, J. H., and Ritz, C.: The crystal fabric of ice from full-waveform borehole sonic logging, *Journal
of Geophysical Research: Earth Surface*, 117, <https://doi.org/10.1029/2012JF002343>, <https://doi.org/10.1029/2012JF002343>, publisher:
John Wiley & Sons, Ltd, 2012.
- Gödert, G.: A mesoscopic approach for modelling texture evolution of polar ice including recrystallization phe-
nomena, *Annals of Glaciology*, 37, 23–28, <https://doi.org/10.3189/172756403781815375>, [https://www.cambridge.
org/core/article/mesoscopic-approach-for-modelling-texture-evolution-of-polar-ice-including-recrystallization-phenomena/
1B280C6F79C63AF5634FAFFFEFA5CA723](https://www.cambridge.org/core/article/mesoscopic-approach-for-modelling-texture-evolution-of-polar-ice-including-recrystallization-phenomena/1B280C6F79C63AF5634FAFFFEFA5CA723), 2003.
- 740 Harte, A., Atkinson, M., Preuss, M., and Fonseca, J.: A statistical study of the relationship between plastic strain and lattice misorientation
on the surface of a deformed Ni-based superalloy, *Acta Materialia*, 195, <https://doi.org/10.1016/j.actamat.2020.05.029>, 2020.
- Hindmarsh, R. C. A.: Thermoviscous stability of ice-sheet flows, *Journal of Fluid Mechanics*, 502, 17–40,
745 <https://doi.org/10.1017/S0022112003007390>, [https://www.cambridge.org/core/article/thermoviscous-stability-of-icesheet-flows/
13E3DB8CEFF97DB4A911E9F174B8E994](https://www.cambridge.org/core/article/thermoviscous-stability-of-icesheet-flows/13E3DB8CEFF97DB4A911E9F174B8E994), 2004.
- Holtzschcher, J. J., G. de Q. Robin, and Glen, J. W.: Depth of Polar Ice Caps, *The Geographical Journal*, 120, 193–202,
<https://doi.org/10.2307/1791535>, <http://www.jstor.org/stable/1791535>, publisher: [Wiley, Royal Geographical Society (with the Institute
of British Geographers)], 1954.
- 750 Hondoh, Takeo: Nature and behavior of dislocations in ice, *Physics of Ice Core Records*, <http://hdl.handle.net/2115/32459>, 2000.
- Hudleston, P. J.: Structures and fabrics in glacial ice: A review, *Journal of Structural Geology*, 81, 1–27,
<https://doi.org/10.1016/j.jsg.2015.09.003>, <http://www.sciencedirect.com/science/article/pii/S0191814115300365>, 2015.
- Humphreys, F. and Hatherly, M.: *Recrystallization and Related Annealing Phenomena*, Pergamon, Oxford, 2004.
- Jacka, T. and Maccagnan, M.: Ice crystallographic and strain rate changes with strain in compression and extension, *Cold Regions
755 Science and Technology*, 8, 269–286, [https://doi.org/10.1016/0165-232X\(84\)90058-2](https://doi.org/10.1016/0165-232X(84)90058-2), [http://www.sciencedirect.com/science/article/pii/
0165232X84900582](http://www.sciencedirect.com/science/article/pii/0165232X84900582), 1984.

- Jacka, T. H.: Flow rates and crystal orientation fabrics in compression of polycrystalline ice at low temperatures and stresses, *Physics of Ice Core Record*, <https://ci.nii.ac.jp/naid/10015735360/en/>, 2000.
- 760 Jiang, D.: Vorticity determination, distribution, partitioning and the heterogeneity and non-steadiness of natural deformations, *Journal of Structural Geology*, 16, 121–130, [https://doi.org/10.1016/0191-8141\(94\)90023-X](https://doi.org/10.1016/0191-8141(94)90023-X), <https://www.sciencedirect.com/science/article/pii/S019181419490023X>, 1994.
- Johnsen, S. J., Dahl-Jensen, D., Dansgaard, W., and Gundestrup, N.: Greenland palaeotemperatures derived from GRIP bore hole temperature and ice core isotope profiles, *Tellus B: Chemical and Physical Meteorology*, 47, 624–629, <https://doi.org/10.3402/tellusb.v47i5.16077>, <https://doi.org/10.3402/tellusb.v47i5.16077>, publisher: Taylor & Francis, 1995.
- 765 Jordan, T. M., Schroeder, D. M., Elsworth, C. W., and Siegfried, M. R.: Estimation of ice fabric within Whillans Ice Stream using polarimetric phase-sensitive radar sounding, *Annals of Glaciology*, 61, 74–83, <https://doi.org/10.1017/aog.2020.6>, <https://www.cambridge.org/core/journals/annals-of-glaciology/article/estimation-of-ice-fabric-within-whillans-ice-stream-using-polarimetric-phasesensitive-radar-sounding/F334B5CE907DBED94E7614EFB32E1DAF>, edition: 2020/02/03 Publisher: Cambridge University Press, 2020.
- 770 Journaux, B., Chauve, T., Montagnat, M., Tommasi, A., Barou, F., Mainprice, D., and Gest, L.: Recrystallization processes, microstructure and crystallographic preferred orientation evolution in polycrystalline ice during high-temperature simple shear, *The Cryosphere*, 13, 1495–1511, <https://doi.org/10.5194/tc-13-1495-2019>, <https://www.the-cryosphere.net/13/1495/2019/>, 2019.
- 775 Jun, L., Jacka, T., and Budd, W.: Deformation rates in combined compression and shear for ice which is initially isotropic and after the development of strong anisotropy, *Annals of Glaciology*, 23, 247–252, <https://doi.org/10.3189/S0260305500013501>, <https://www.cambridge.org/core/article/deformation-rates-in-combined-compression-and-shear-for-ice-which-is-initially-isotropic-and-after-the-development-of-strong-anisotropy/87ABC4DFAFFA123128C6CA2E883CAE6E>, edition: 2017/01/20 Publisher: Cambridge University Press, 1996.
- Kamb, B.: Experimental Recrystallization of Ice Under Stress, in: *Flow and Fracture of Rocks*, pp. 211–241, American Geophysical Union (AGU), <https://doi.org/10.1029/GM016p0211>, <https://agupubs.onlinelibrary.wiley.com/doi/abs/10.1029/GM016p0211>, 1972.
- 780 Kennedy, J. H. and Pettit, E. C.: The response of fabric variations to simple shear and migration recrystallization, *Journal of Glaciology*, 61, 537–550, <https://doi.org/10.3189/2015JoG14J156>, <https://www.cambridge.org/core/journals/journal-of-glaciology/article/response-of-fabric-variations-to-simple-shear-and-migration-recrystallization/CFE83A878F70F5F8E7135C28A77FF9C0>, 2015.
- 785 Kluskiewicz, D., WADDINGTON, E., Anandakrishnan, S., Voigt, D., Matsuoka, K., and McCARTHY, M.: Sonic methods for measuring crystal orientation fabric in ice, and results from the West Antarctic ice sheet (WAIS) Divide, *Journal of Glaciology*, 63, 1–15, <https://doi.org/10.1017/jog.2017.20>, 2017.
- Llorens, M.-G., Grier, A., Bons, P. D., Lebensohn, R. A., Evans, L. A., Jansen, D., and Weikusat, I.: Full-field predictions of ice dynamic recrystallisation under simple shear conditions, *Earth and Planetary Science Letters*, 450, 233–242, <https://doi.org/10.1016/j.epsl.2016.06.045>, <http://www.sciencedirect.com/science/article/pii/S0012821X16303326>, 2016.
- 790 Llorens, M.-G., Grier, A., Steinbach, F., Bons, P. D., Gomez-Rivas, E., Jansen, D., Roessiger, J., Lebensohn, R. A., and Weikusat, I.: Dynamic recrystallization during deformation of polycrystalline ice: insights from numerical simulations, *Philosophical Transactions of the Royal Society A: Mathematical, Physical and Engineering Sciences*, 375, 20150346, <https://doi.org/10.1098/rsta.2015.0346>, <https://royalsocietypublishing.org/doi/abs/10.1098/rsta.2015.0346>, 2017.

- Martin Alnæs, Jan Blechta, Johan Hake, August Johansson, Benjamin Kehlet, Anders Logg, Chris Richardson, Johannes Ring, Marie E Rognes, and Garth N Wells: The FEniCS Project Version 1.5, *Archive of Numerical Software*, 3, 9–23, 795 <https://doi.org/10.11588/ans.2015.100.20553>, 2015.
- Martín, C., Gudmundsson, G. H., Pritchard, H. D., and Gagliardini, O.: On the effects of anisotropic rheology on ice flow, internal structure, and the age-depth relationship at ice divides, *Journal of Geophysical Research: Earth Surface*, 114, <https://doi.org/10.1029/2008JF001204>, <https://doi.org/10.1029/2008JF001204>, publisher: John Wiley & Sons, Ltd, 2009.
- Matsuoka, K., Furukawa, T., Fujita, S., Maeno, H., Uratsuka, S., Naruse, R., and Watanabe, O.: Crystal orientation fabrics within the Antarctic ice sheet revealed by a multipolarization plane and dual-frequency radar survey, *Journal of Geophysical Research: Solid Earth*, 108, 800 <https://doi.org/10.1029/2003JB002425>, <https://doi.org/10.1029/2003JB002425>, publisher: John Wiley & Sons, Ltd, 2003.
- Meyer, C. R. and Minchew, B. M.: Temperate ice in the shear margins of the Antarctic Ice Sheet: Controlling processes and preliminary locations, *Earth and Planetary Science Letters*, 498, 17–26, <https://doi.org/10.1016/j.epsl.2018.06.028>, <http://www.sciencedirect.com/science/article/pii/S0012821X18303790>, 2018.
- 805 Minchew, B., Meyer, C., Robel, A., Gudmundsson, G., and Simons, M.: Processes controlling the downstream evolution of ice rheology in glacier shear margins: case study on Rutford Ice Stream, West Antarctica, *Journal of Glaciology*, 64, 1–12, <https://doi.org/10.1017/jog.2018.47>, 2018.
- Montagnat, M., Löwe, H., Calonne, N., Schneebeli, M., Matzl, M., and Jaggi, M.: On the Birth of Structural and Crystallographic Fabric Signals in Polar Snow: A Case Study From the EastGRIP Snowpack, *Frontiers in Earth Science*, 8, 365, 810 <https://doi.org/10.3389/feart.2020.00365>, 2020.
- Mouginot, J., Rignot, E., and Scheuchl, B.: Continent-Wide, Interferometric SAR Phase, Mapping of Antarctic Ice Velocity, *Geophysical Research Letters*, 46, 9710–9718, <https://doi.org/10.1029/2019GL083826>, <https://doi.org/10.1029/2019GL083826>, publisher: John Wiley & Sons, Ltd, 2019.
- Passchier, C.: The classification of dilatant flow types, *Journal of Structural Geology*, 13, 101–104, [https://doi.org/10.1016/0191-8141\(91\)90105-R](https://doi.org/10.1016/0191-8141(91)90105-R), <http://www.sciencedirect.com/science/article/pii/019181419190105R>, 1991.
- 815 Paterson, W. S. B.: *The Physics of Glaciers*, Pergamon, Oxford, 3rd edn., 1999.
- Pattyn, F., Perichon, L., Aschwanden, A., Breuer, B., de Smedt, B., Gagliardini, O., Gudmundsson, G. H., Hindmarsh, R. C. A., Hubbard, A., Johnson, J. V., Kleiner, T., Konovalov, Y., Martin, C., Payne, A. J., Pollard, D., Price, S., Rückamp, M., Saito, F., Souček, O., Sugiyama, S., and Zwinger, T.: Benchmark experiments for higher-order and full-Stokes ice sheet models (ISMIP–HOM), *The Cryosphere*, 2, 95–108, 820 <https://doi.org/10.5194/tc-2-95-2008>, <https://www.the-cryosphere.net/2/95/2008/>, publisher: Copernicus Publications, 2008.
- Piazolo, S., Bons, P., and Passchier, C.: The influence of matrix rheology and vorticity on fabric development of populations of rigid objects during plane strain deformation, *Tectonophysics*, 351, 315–329, [https://doi.org/10.1016/S0040-1951\(02\)00220-2](https://doi.org/10.1016/S0040-1951(02)00220-2), <https://www.sciencedirect.com/science/article/pii/S0040195102002202>, 2002.
- Piazolo, S., Jessell, M. W., Prior, D. J., and Bons, P. D.: The integration of experimental in-situ EBSD observations and numerical simulations: a novel technique of microstructural process analysis, *Journal of Microscopy*, 213, 273–284, <https://doi.org/10.1111/j.0022-2720.2004.01304.x>, <https://doi.org/10.1111/j.0022-2720.2004.01304.x>, publisher: John Wiley & Sons, Ltd, 2004.
- 825 Piazolo, S., Wilson, C. J. L., Luzin, V., Brouzet, C., and Peternell, M.: Dynamics of ice mass deformation: Linking processes to rheology, texture, and microstructure, *Geochemistry, Geophysics, Geosystems*, 14, 4185–4194, <https://doi.org/10.1002/ggge.20246>, <https://doi.org/10.1002/ggge.20246>, 2013.

- 830 Piazzolo, S., Montagnat, M., Grennerat, F., Moulinec, H., and Wheeler, J.: Effect of local stress heterogeneities on dislocation fields, examples from transient creep in polycrystalline ice, 90, 303–309, <https://doi.org/10.1016/j.actamat.2015.02.046>, <http://www.scopus.com/inward/record.url?scp=84925256590&partnerID=8YFLogxK>, 2015.
- Pimienta, P. and Duval, P.: Mechanical behavior of anisotropic polar ice, *The Physical Basis of Ice Sheet Modelling*, 170, 1987.
- Placidi, L., Greve, R., Seddik, H., and Faria, S. H.: Continuum-mechanical, Anisotropic Flow model for polar ice masses, based on an
835 anisotropic Flow Enhancement factor, *Continuum Mechanics and Thermodynamics*, 22, 221–237, <https://doi.org/10.1007/s00161-009-0126-0>, <https://doi.org/10.1007/s00161-009-0126-0>, 2010.
- Qi, C., Goldsby, D. L., and Prior, D. J.: The down-stress transition from cluster to cone fabrics in experimentally deformed ice, *Earth and Planetary Science Letters*, 471, 136–147, <https://doi.org/10.1016/j.epsl.2017.05.008>, <http://www.sciencedirect.com/science/article/pii/S0012821X17302625>, 2017.
- 840 Qi, C., Prior, D. J., Craw, L., Fan, S., Llorens, M.-G., Griera, A., Negrini, M., Bons, P. D., and Goldsby, D. L.: Crystallographic preferred orientations of ice deformed in direct-shear experiments at low temperatures, *The Cryosphere*, 13, 351–371, <https://doi.org/10.5194/tc-13-351-2019>, <https://www.the-cryosphere.net/13/351/2019/>, 2019.
- Richards, D. H., Pegler, S. S., Piazzolo, S., and Harlen, O. G.: The evolution of ice fabrics: A continuum modelling approach validated against laboratory experiments, *Earth and Planetary Science Letters*, 556, 116–118, <https://doi.org/10.1016/j.epsl.2020.116718>, <http://www.sciencedirect.com/science/article/pii/S0012821X20306622>, 2021.
- 845 Rongen, M., Bay, R. C., and Blot, S.: Observation of an optical anisotropy in the deep glacial ice at the geographic South Pole using a laser dust logger, *The Cryosphere*, 14, 2537–2543, <https://doi.org/10.5194/tc-14-2537-2020>, <https://tc.copernicus.org/articles/14/2537/2020/>, publisher: Copernicus Publications, 2020.
- Schytt, V.: Snow and ice studies in Antarctica, Norwegian-British-Swedish antarctic expedition, 1949-52. Scientific results, pp. S. 9–148,
850 3 pl.–bl., 6, 8 pl.–s., 1 diag.–bl., <http://urn.kb.se/resolve?urn=urn:nbn:se:su:diva-75505>, number Of Volumes: Vol. 4. A-C Place: Oslo Publisher: Norsk Polarsinstitutt, 1958.
- Shepherd, A., Ivins, E., Rignot, E., Smith, B., van den Broeke, M., Velicogna, I., Whitehouse, P., Briggs, K., Joughin, I., Krinner, G., Nowicki, S., Payne, T., Scambos, T., Schlegel, N., A. G., Agosta, C., Ahlstrøm, A., Babonis, G., Barletta, V., Blazquez, A., Bonin, J., Csatho, B., Cullather, R., Felikson, D., Fettweis, X., Forsberg, R., Gallee, H., Gardner, A., Gilbert, L., Groh, A., Gunter, B., Hanna, E.,
855 Harig, C., Helm, V., Horvath, A., Horvath, M., Khan, S., Kjeldsen, K. K., Konrad, H., Langen, P., Lecavalier, B., Loomis, B., Luthcke, S., McMillan, M., Melini, D., Mernild, S., Mohajerani, Y., Moore, P., Mouginit, J., Moyano, G., Muir, A., Nagler, T., Nield, G., Nilsson, J., Noel, B., Ootaka, I., Pattle, M. E., Peltier, W. R., Pie, N., Rietbroek, R., Rott, H., Sandberg-Sørensen, L., Sasgen, I., Save, H., Scheuchl, B., Schrama, E., Schröder, L., Seo, K.-W., Simonsen, S., Slater, T., Spada, G., Sutterley, T., Talpe, M., Tarasov, L., van de Berg, W. J., van der Wal, W., van Wessem, M., Vishwakarma, B. D., Wiese, D., Wouters, B., and The IMBIE team: Mass balance of the Antarctic Ice
860 Sheet from 1992 to 2017, *Nature*, 558, 219–222, <https://doi.org/10.1038/s41586-018-0179-y>, <https://doi.org/10.1038/s41586-018-0179-y>, 2018.
- Steinemann, S.: Experimentelle Untersuchungen zur Plastizität von Eis, Ph.D. thesis, ETH Zurich, <https://doi.org/10.3929/ethz-a-000096707>, 1958.
- Stoll, N., Weikusat, I., Kerch, J., Kleitz, I., Eichler, J., Shigeyama, W., Homma, T., Jansen, D., Bayer-Giraldi, M., Kuiper, E.-J., Westhoff, J.,
865 Saruya, T., Faria, S. H., Kipfstuhl, S., and Dahl-Jensen, D.: Physical properties of the NEGIS ice core - The upper 1700m in EGRIP, in: *The Ninth Symposium on Polar Science*, National Institute of Polar Research (NIPR), Tokyo, Japan, <https://epic.awi.de/id/eprint/48741/>, 2018.

- Svendsen, B. and Hutter, K.: A continuum approach for modelling induced anisotropy in glaciers and ice sheets, *Annals of Glaciology*, 23, 262–269, <https://doi.org/10.3189/S0260305500013525>, <https://www.cambridge.org/core/journals/annals-of-glaciology/article/continuum-approach-for-modelling-induced-anisotropy-in-glaciers-and-ice-sheets/16FE39C48B194C4D0E8ABB97A54F99A5>, 1996.
- 870 ten Grotenhuis, S. M., Piazzolo, S., Pakula, T., Passchier, C. W., and Bons, P. D.: Are polymers suitable rock analogs?, *Tectonophysics*, 350, 35–47, [https://doi.org/10.1016/S0040-1951\(02\)00080-X](https://doi.org/10.1016/S0040-1951(02)00080-X), <https://www.sciencedirect.com/science/article/pii/S004019510200080X>, 2002.
- Tikoff, B. and Fossen, H.: The limitations of three-dimensional kinematic vorticity analysis, *Journal of Structural Geology*, 17, 1771–1784, [https://doi.org/10.1016/0191-8141\(95\)00069-P](https://doi.org/10.1016/0191-8141(95)00069-P), <http://www.sciencedirect.com/science/article/pii/019181419500069P>, 1995.
- 875 Treverrow, A., Warner, R. C., Budd, W. F., and Craven, M.: Meteoric and marine ice crystal orientation fabrics from the Amery Ice Shelf, East Antarctica, *Journal of Glaciology*, 56, 877–890, <https://doi.org/10.3189/002214310794457353>, <https://www.cambridge.org/core/article/meteoric-and-marine-ice-crystal-orientation-fabrics-from-the-amery-ice-shelf-east-antarctica/65BE624208F39BEAF47F947520B45DAA>, 2010.
- van der Veen, C. and Whillans, I.: Development of fabric in ice, *Cold Regions Science and Technology*, 22, 171–195, [https://doi.org/10.1016/0165-232X\(94\)90027-2](https://doi.org/10.1016/0165-232X(94)90027-2), <http://www.sciencedirect.com/science/article/pii/0165232X94900272>, 1994.
- 880 Wilson, C. J. and Peterzell, M.: Ice deformed in compression and simple shear: control of temperature and initial fabric, *Journal of Glaciology*, 58, 11–22, <https://doi.org/10.3189/2012JoG11J065>, 2012.
- Wilson, C. J. L.: Experimental work on the effect of pre-existing anisotropy on fabric development in glaciers, *Geological Society, London, Special Publications*, 176, 97, <https://doi.org/10.1144/GSL.SP.2000.176.01.08>, <http://sp.lyellcollection.org/content/176/1/97.abstract>, 2000.
- 885 Xypolias, P.: Vorticity analysis in shear zones: A review of methods and applications, *Structural Diagenesis*, 32, 2072–2092, <https://doi.org/10.1016/j.jsjg.2010.08.009>, <http://www.sciencedirect.com/science/article/pii/S0191814110001392>, 2010.